The ROSAT High Resolution Imager (HRI) Calibration Report

U.S. ROSAT SCIENCE DATA CENTER/SAO

rsdc@cfa.harvard.edu

Revised 1997 June 1

html address: http://hea-www.harvard.edu/rosat/rsdc_www/HRI_CAL_REPORT/hri.html

Original Authors

David, L.P.
Harnden, F.R.
Kearns, K.E.
Zombeck, M.V.

Contributors to revisions

Harris, D.E.
Prestwich, A.
Primini, F.A.
Silverman, J.D.
Snowden, S.L.

CHANGE DOC

96 Feb 01

Minor Revisions
- Effective Area (Sec 3.3)
- HV Increase (Sec 3.8)

Substantive Revisions
- Spectral Response (Sec 3.5)
- UV Response (Sec 3.6)

New Material
- Hotspots (Sec 3.9)
- Point Source Sensitivity (4.2)

New Figures
- Mean Pulse Height Channel (Fig. 18)
- Existence of a Source (Fig. 27)

97 Feb 15

Substantive Revisions
- Spectral Response (Sec 3.5)
- UV Response (Sec 3.6)
- Table 7

New Figures
- Time History of Detector Gain (Fig. 20)
- Spectral Model Fit to PHA (Fig. 21)
- Spectral Gain Calibration (Fig. 22)

97 Jun 1

Substantive Revisions
- Expected Count Rates (Sec 4.3)

New material
- High Voltage Increase (Sec 3.8)
- Flux of a Source - Gaussian Statistics Case (Sec 4.2.1)

New Figures
- Minimum detectable source flux (Fig. 26)
- ECF plot-Powerlaw spectral model (Fig. 28)
- ECF plot-Thermal Bremsstrahlung spectral model (Fig. 29)
- ECF plot-Raymond-Smith spectral model (Fig. 30)
- ECF plot-Blackbody spectral model (Fig. 31)

Contents

1. Lists of Figures and Tables

Figures

Tables

2. Overview

For purposes of planning HRI observations (and of analyzing data as well), the performance of the combined HRI and ROSAT XRT (X-Ray Telescope) is described in this report, which is based upon laboratory, ground-based, and in-flight data.

The HRI information in this document supersedes that in previously issued versions of the "ROSAT Mission Description" (e.g., APPENDIX F of the U.S. announcement NRA 91-OSSA-3; references below to "Appendix F" refer to the version dated "January 1991"). It has been reorganized to some extent in order to improve the clarity of presentation. To assist those familiar with Appendix F, the following concordance is provided for finding updated material corresponding to sections of that appendix:

This document	Appendix F section
2. OVERVIEW	4.3.1
3. Performance	4.3.2
3.1 Detector Geometry	4.3.2.1
3.2 Spatial Response	4.3.2.4
3.3 Effective Area	4.3.2.2, 11.1
3.4 Background	4.3.2.6, 7.8.3
3.5 Spectral Response	none (i.e., new)
3.6 UV Response	4.3.2.3
3.7 Event Timing	4.3.2.5
4. Feasibility of observations	11.
4.1 General Assumptions	11.1
4.2 Point Source Sensitivity	11.2, 11.5
4.3 Expected Count Rates	11.3
4.3.1 Examples	11.3.1
4.4 Time Variability Studies	11.6
4.5 Comparison to the Einstein HRI	11.7

3. Performance

The ROSAT High Resolution Imager (HRI) is very similar to the Einstein Observatory HRI and is comprised of two cascaded microchannel plates (MCPs) with a crossed grid position readout system. The detector performance can be characterized by such parameters as those listed in Table 4.3 of Appendix F. Two significant changes from the Einstein instrument that have affected the performance of the detector are: the substitution of CsI for MgF_2 as the detector photocathode, and the introduction of a thin aluminum-coated plastic membrane (the "electrostatic shield") near the front MCP (in addition to the UV/Ion shield which is situated farther in front of the detector).

3.1. Detector Geometry

3.1.1. Field of View

The 36mm-diameter HRI MCPs have a holding-fixture open aperture diameter of 30mm, and the readout system has a working area of 27mm x 27mm. Hence the net useful field of view is given by the intersection of the circular MCP and square readout, as shown in Figure 4.9 of Appendix F. The CsI photocathode used in the HRI is evaporated in the pattern shown in Figure 4.9, so that there are four small "tabs" of uncoated MCP area which are used to monitor the stability of the photocathode.

3.1.2. Plate Scale

The Andromeda galaxy (M31) was observed for 50 ks, with numerous point sources detected. With 12 identified sources distributed over the HRI field from this observation (data courtesy of F. Primini), the mean plate scale determined with a standard astrometric plate reduction method was found to be:

$$0.499 \pm 0.001 \text{ arc seconds per pixel}$$

(Note that there are 8192 such "pixels" in the "sky-coordinate" event lists distributed to ROSAT HRI observers.)

The relationship between Einstein and ROSAT pixels was also measured (using 23 M31 sources that were matched to Einstein HRI detections) and found to be:

$$1 \text{ ROSAT pixel} = 1.0050 \pm 0.0007 \text{ Einstein pixel}$$

3.2. Spatial Response

3.2.1. Absolute Positions

The process of determining boresight offsets (systematic zero-point shifts found by comparing measured and known positions of catalogued objects) for the HRI has led to the conclusion that there are time-varying errors in the attitude solutions used to correct event positions. Although most known objects are detected at positions within $10''$ of their catalog positions, residual discrepancies can be present even after application of the boresight corrections. This can be particularly evident in a comparison of observations of the same object taken six months apart (and hence at spacecraft roll angles differing by 180 degrees).

Compensation for such effects is possible whenever X rays are detected from previously known objects whose positions have been accurately catalogued.

3.2.2. Preflight measurements

The pre-launch HRI positional resolution was measured in the lab using a shadow mask with a test pattern consisting of alternating bars of open and closed area of various widths, as shown in Figures 4.13 and 4.14 of Appendix F. Mean values from such measurements gives $\sigma = 8.4\mu$m, which at the ROSAT X-ray telescope focal length of 2.4 m, yields an intrinsic FWHM resolution of $1.7''$ for the HRI.

Large scale geometrical distortions of the HRI were measured by projecting a mesh pattern on the face of the detector (cf. Appendix F and its Figure 4.15 for details) and found to be less than $1''$ over its field of view. Note, however, that the image resolution varies over the field due to the off-axis response of the X-ray Telescope. Small-scale differential nonlinearity was also determined to have an RMS deviation from the mean of less than $\approx 0.1''$.

3.2.3. In-flight Point Spread Functions (PSF)

The PSF describes the surface brightness distribution of imaged point sources. There are three significant components: the XRT PSF, the HRI PSF, and a residual blurring attributable to the aspect correction (often discernible as a small ellipsoidal component).

On-Axis PSF

Although the XRT PSF has a central core with a FWHM of $3''$ (as determined by ground test), microroughness in the mirror surfaces leads to a slight but measurable scattering of X rays and produces a small energy-dependent tail or wing in the PSF. As determined by ground test measurements, the fraction of imaged photons in the tail (beyond $10''$) of the image of a point source is given in Table 1.

Table 1
Energy dependence of the mirror-scattering

E (keV)	% photons outside a 10″ radius
0.18	0.7
0.28	1.3
0.93	6.0
1.49	11.0
1.70	13.3

The HRI PSF has a central core with a FWHM of 1.7″ (as determined in the laboratory). In the absence of the electrostatic shield, the PSF has a near-Gaussian shape, but the electrostatic shield (introduced to reduce the background count rate) has broadened the PSF, creating a so-called "halo". X-rays interacting in the interchannel web in front of the MCPs produce electrons that are "captured" in microchannel pores a considerable distance from the initial event site, initiating an electron avalanche leading to a false position. Although the region between the shield and the MCP is, to first order, field free, fringe electrostatic fields deflect the web electrons back into the MCP. The magnitude of the effect is predicted to decrease with increasing energy, whereas mirror scattering increases with energy.

The in-flight, on-axis PSF, which includes aspect solution effects, has been determined from a 9.1 ks exposure of HZ43 which yielded 109,000 net counts. Figure 1 shows the azimuthally averaged surface brightness profile of this observation. The HRI halo is obvious in Figure 1 and dominates the PSF beyond approximately 15″. The solid curve is a parametric representation of the in-flight, on-axis, PSF and consists of the sum of two Gaussians and an exponential. This functional form for the azimuthally averaged PSF, provides a good description of the PSF out to a radius of 2′, and is given by:

$$PSF(R) = A_1 e^{-0.5(\frac{R}{S_1})^2} + A_2 e^{-0.5(\frac{R}{S_2})^2} + A_3 e^{\frac{-R}{S_3}}$$

where the radial distance, R, is in arc seconds, and:

$$\begin{array}{ll} A_1 = 0.9638 & S_1 = 2.1858 \text{ arcsec} \\ A_2 = 0.1798 & S_2 = 4.0419 \text{ arcsec} \\ A_3 = 0.00090 & S_3 = 31.69 \text{ arcsec} \end{array}$$

Note the arbitrary normalization of the above expression for the azimuthally-averaged surface brightness. Figure 1 shows that there is an additional component in the PSF beyond 2′, but this component will be well below the background in most observations. We have not fit this additional component, since we do not know at present how strongly it depends on energy.

The azimuthally averaged surface brightness for on-axis observations of HZ43, AR Lac, and LMC X-1 is shown in Figure 2. Since these sources represent a wide range of mean X-ray energies, this figure demonstrates that the combined PSF (HRI/XRT) is largely energy independent within 2′.

The integrated surface brightness (encircled energy function) for the long HZ43 observation is shown in Figure 3. The extended HRI halo is evident in this figure and shows that approximately 15% of the total power is scattered beyond 10″, 7% beyond 1′, and less than 1% beyond 5′. Figure 4 shows the encircled energy function for HZ43, Ar Lac, and LMC X-1. This figure shows that the encircled energy function is consistent within the statistical errors for these three sources, and is not strongly dependent on the photon energy.

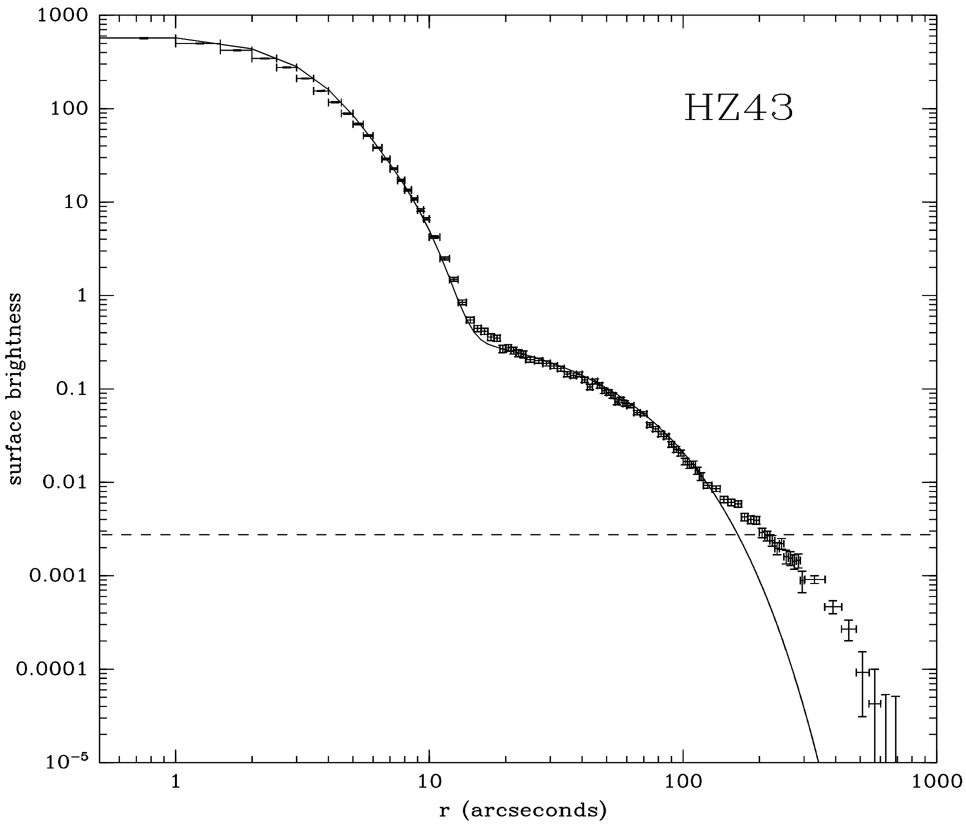

Fig. 1. The point spread function from a long exposure of HZ43. The surface brightness is in units of counts per pixel. To improve the statistics, the data were binned in increasingly larger annuli (0.5, 1, 2, 4, 10, and 60 arcseconds). The dashed line is the background rate in this observation determined between $8'$ and $12'$ off-axis. Also shown is the parametric form for the PSF.

The on-axis PSF given above is based on a single long observation of HZ43 with excellent photon statistics. Such an observation is required in order to accurately parameterize the HRI halo. We have also looked at a number of shorter (nearly on-axis) observations of HZ43, AR Lac, LMC X-1, and the Meaty Source taken throughout the mission in order to determine the reproducibility of the on-axis PSF. In general, there is no difference (within the statistics) beyond $10''$. This indicates that the HRI halo is stable and approximately energy independent. However, due to random errors in the aspect solution, the width of the core of the HRI images can vary. Fitting the above functional form of the PSF to this sample (treating the width and normalizations of the two gaussians as free parameters) shows that the best fit value of S1 varies from $1.9''$ to $2.5''$, and the best fit value S2 of varies from $3.5''$ to $4.1''$ (see Fig. 5). Variations in S1 and S2 between observations of the same source (e.g., the Meaty Source) span almost the entire range of values shown in Figure 5.

Residual errors in the aspect solution also occasionally produce asymmetrical features in the PSF. Figure 6 displays images of the so-called "Meaty Source" (a white dwarf star discovered with the WFC) illustrating the inner core's appearance when the aspect solution is correct and when there are errors leading to an ellipsoidal image. The major axis of the

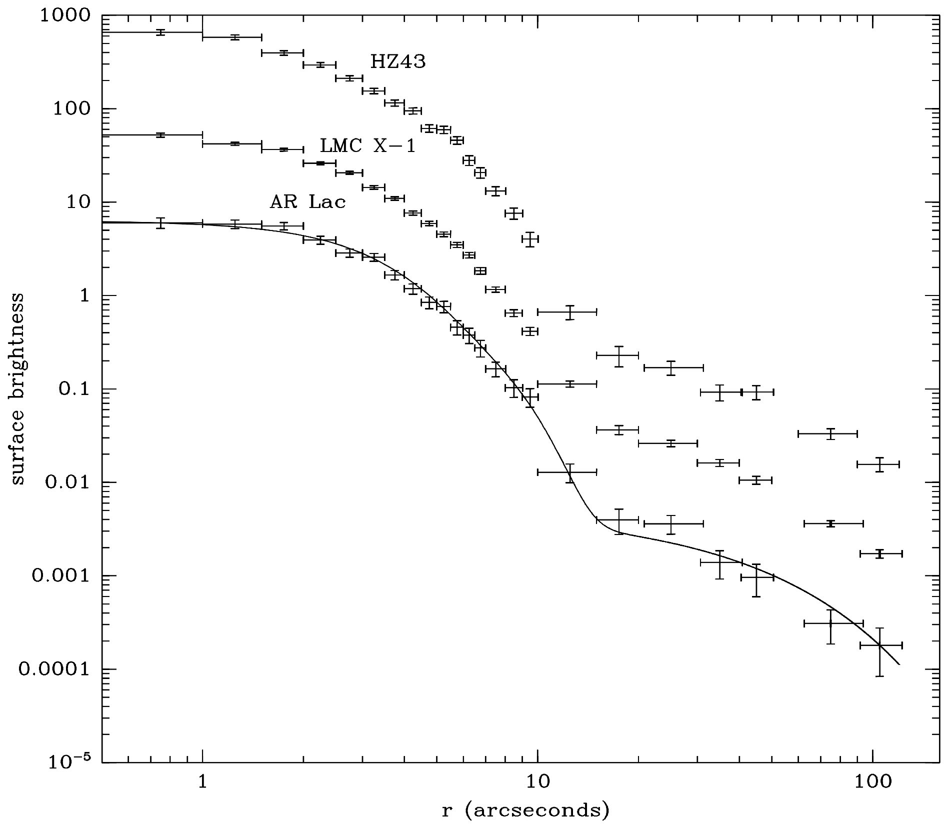

Fig. 2. A comparison of the point spread functions of HZ43, LMC X-1, and AR Lac with arbitrary normalization. To improve the statistics, the data were binned in increasingly larger annuli (0.5, 1, 2, 5, 10, and 30 arcseconds). Also shown is the parametric form for the PSF normalized to the AR Lac observation.

ellipsoidal images are not aligned with the wobble direction. The asymmetry is the strongest between $5''$ and $10''$ from the centroid of the image and can have amplitudes up to 30%. When possible, the user should use the image of a known point source within $5'$ of their target as a template for the HRI PSF.

The actual two-dimensional PSF has a 16-fold-symmetrical pattern ("radial spokes") caused by the shadowing of mirror-scattered X rays by the mirror-support structure, as well as an ellipsoidal component due to an imperfect aspect solution. The radial spokes should only appear in images with large numbers of detected photons in observations which are not "wobbled".

Off-Axis PSF

The spatial resolution of the HRI off-axis is dominated by the XRT PSF which degrades rapidly with increasing off-axis angle. Figures 7 and 8 display several off-axis pointings of HZ43 and LMC X-1, and illustrate how the images change with off-axis angle. Figure 9 shows contours of the HZ43 images. The images were first smoothed with a gaussian filter with $\sigma = 1''$ ($\theta \leq 6.0'$), $\sigma = 2''$ ($8.6' \leq \theta \leq 12.0'$), and $\sigma = 4''$ ($13.5' \leq \theta$). These images show that the PSF starts to degrade beyond $5'$ off-axis. Beyond $12'$, the images become

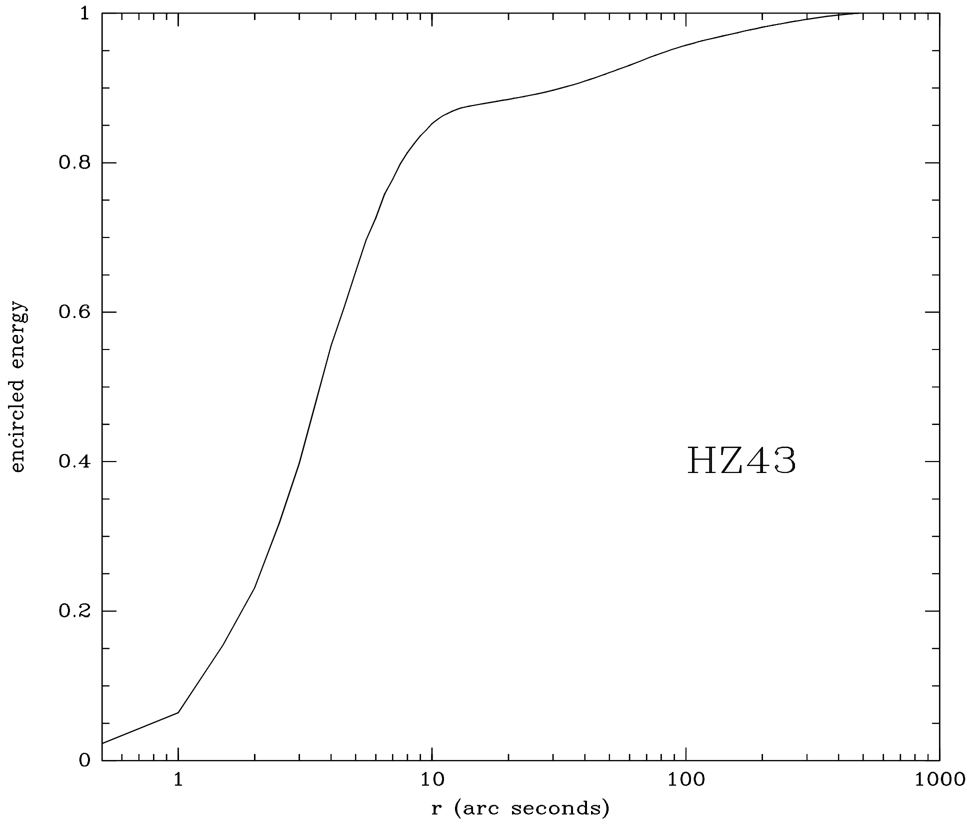

Fig. 3. The on-axis encircled energy function from a long exposure of HZ43. The profile has been normalized to unity at $8'$. This figure shows that approximately 15% of the power is scattered beyond $10''$, 7% is scattered beyond $1'$, and less than 1% is scattered beyond $5'$.

very asymmetrical. A central "bar" in the images well off-axis is perpendicular to a line connecting the optical axis and the image centroid.

The 50% power radius was determined for a series of off-axis pointings of HZ43, AR Lac, and LMC X-1. The asymmetry at large angles has been ignored and the 50% power radius has been computed from radial binning about the image centroids. Figure 10 is a plot of the 50% power radius as a function of off-axis angle for these sources. The solid curve is the best-fit to the following parametric representation of the 50% power radius.

$$r_{50} = \frac{2.35}{2}[\sigma_{HRI}^2 + \sigma_{aspect}^2 + (\sigma_{mirror} + a\theta^b)^2]^{0.5} \text{ arcsec}$$

where θ is given in arc minutes, with the following values for the parameters:

$$\begin{aligned} \sigma_{HRI} &= 0.74'' \\ \sigma_{aspect} &= 1.0'' \\ \sigma_{mirror} &= 1.3'' \\ \text{a} &= 0.0205 \\ \text{b} &= 2.349 \end{aligned}$$

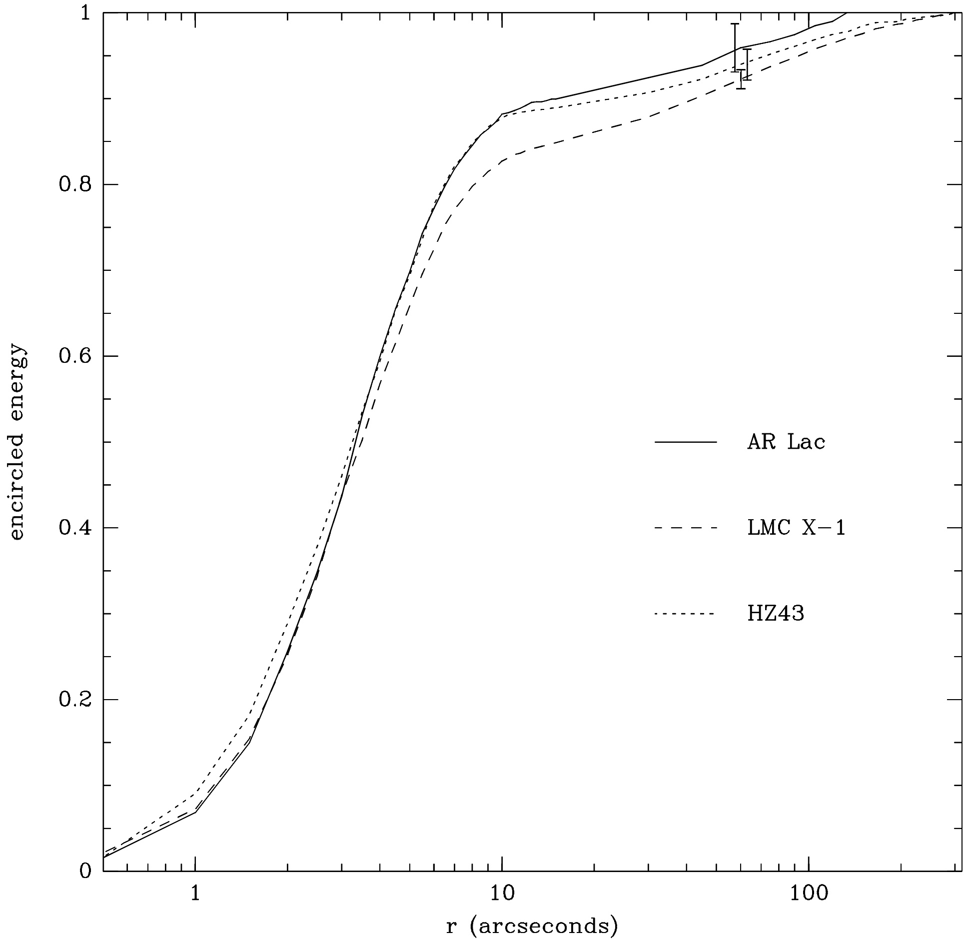

Fig. 4. A comparison of the on-axis encircled energy functions for observations of HZ43, LMC X-1, and AR Lac. Some extended emission is evident in the profile of LMC X-1. The error bars shown in the figure were all evaluated at $1'$, but were offset slightly on the graph for clarity.

It is best to use a circle of radius r_{50} when extracting counts of a source detected off-axis. The total net count rate (corrected for scattering) is then simply twice the net count rate within r_{50}.

A parametric representation of the azimuthally averaged off-axis HRI PSF has also been derived which is a simple extension of the on-axis expression. To determine the off-axis PSF we generated surface brightness profiles for 8 observations of HZ43, spanning a range from $2'$ to $16'$ off-axis. The peak surface brightness was used as the origin, since this generates a monotonically decreasing profile. The set of 8 HZ43 surface brightness profiles were first fit to the on-axis PSF, treating the normalization and width of the two gaussians as free parameters (the photon statistics in these data were insufficient to fit the exponential term). We found that the best fit values of the smaller gaussian were essentially independent of the angle off-axis. We then refit the set of 8 profiles treating only the width of the broader gaussian as a free parameter. The best fit values of s2 are well parameterized by a cubic polynomial in the off-axis angle, and are given by

$$S2 = 3.3 + 0.019\theta - 0.016\theta^2 + 0.0044\theta^3$$

where theta is the angle off-axis in arc minutes. Substituting this expression into the

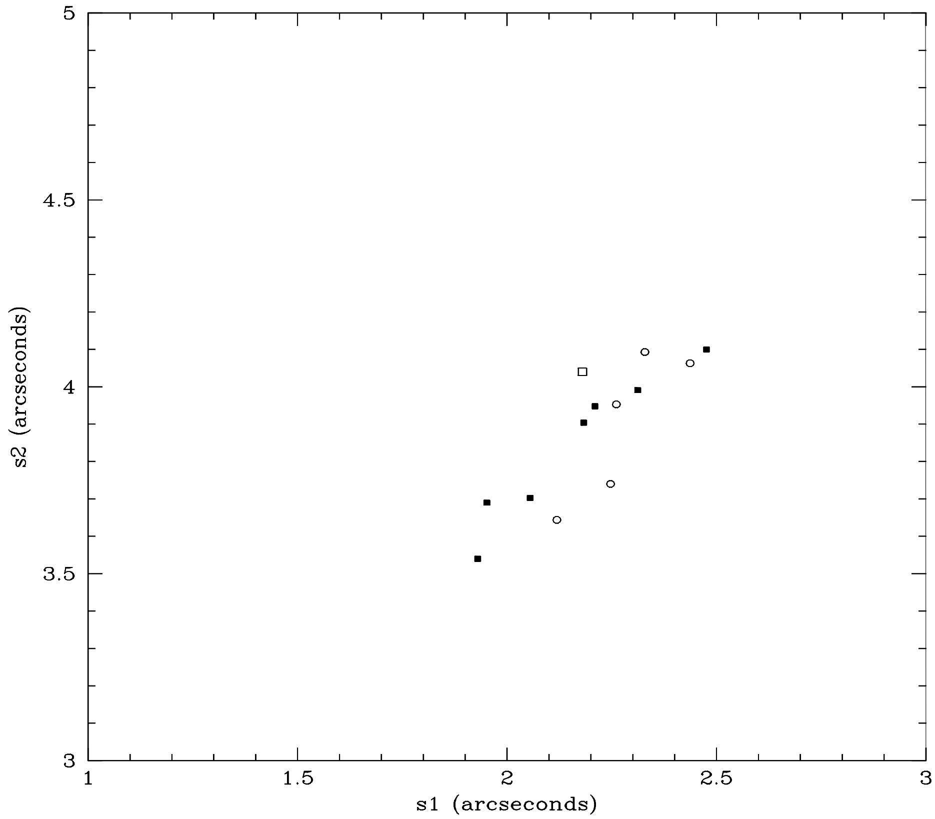

Fig. 5. The best fit values of S1 and S2 to a sample of point sources observed nearly on-axis (within $3'$). The pair of values in the on-axis PSF given above is shown as an open square. Observations of the Meaty Source are indicated by open circles.

on-axis HRI PSF gives the general off-axis representation.

NB: We do not force this expression to reproduce the on-axis value given above. The fact that this expression gives $S2 = 3.3$ for $\theta = 0$, compared to the on-axis value of 4.0 given above, reflects the variation in aspect quality from observation to observation.

Users should note that point sources observed off-axis exhibit significant amounts of non-azimuthal symmetry. The above expression is useful for determining scattering corrections and for use in detect algorithms, but should not be used for image deconvolution. There are a large number of sequences in the PROS calibration directory xrcal containing several objects observed at different angles off-axis. The actual HRI data should be used for any two-dimensional image deconvolution.

3.3. Effective Area

The effective area of the HRI/XRT is the product of the HRI quantum efficiency and the XRT collecting area. The XRT collecting area has been determined from ground tests with the PSPC. The HRI quantum efficiency was also determined in ground tests.

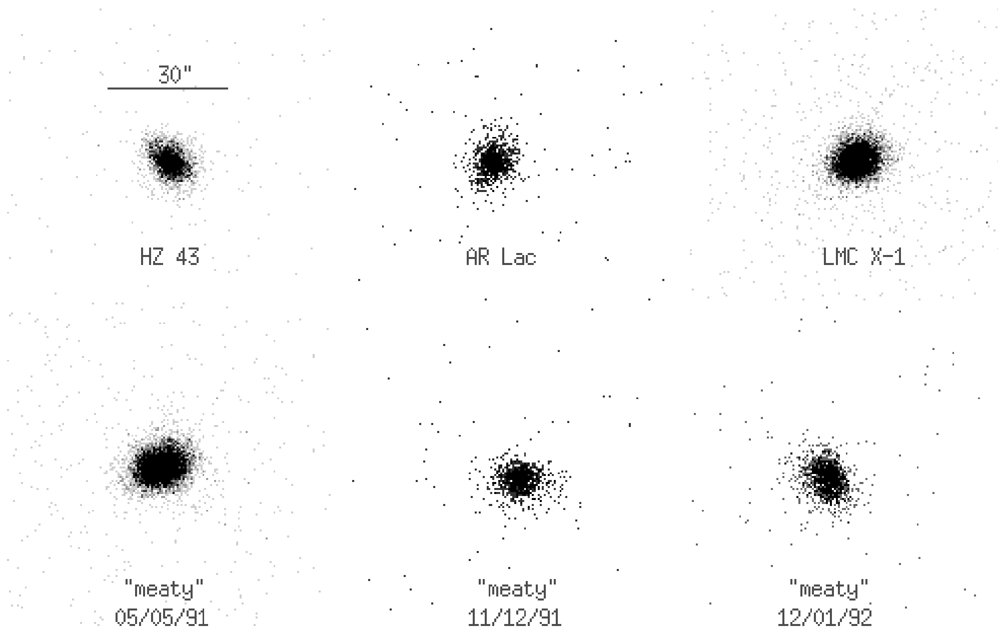

Fig. 6. Comparison of several nearly on-axis (within a few arcminutes) HRI images of point sources. While the core of the images are symmetrical, the surface brightness between $5'' - 8''$ can exhibit some asymmetry. This feature is randomly oriented (i.e., it is not in the direction of the wobble) and depends on the date of the observation. The three images at the bottom of the figure show the WFC "Meaty Source" observed at three different times. Notice that the asymmetry is present in the first and last observation, but not in the intermediate observation.

3.3.1. On-axis Effective Area

Figure 11 (which appeared as Figure 11.1 of Appendix F) is a plot of the on-axis effective area of the HRI/XRT as a function of incident energy; this function is tabulated in Table 2 (Table 11.1 of Appendix F).

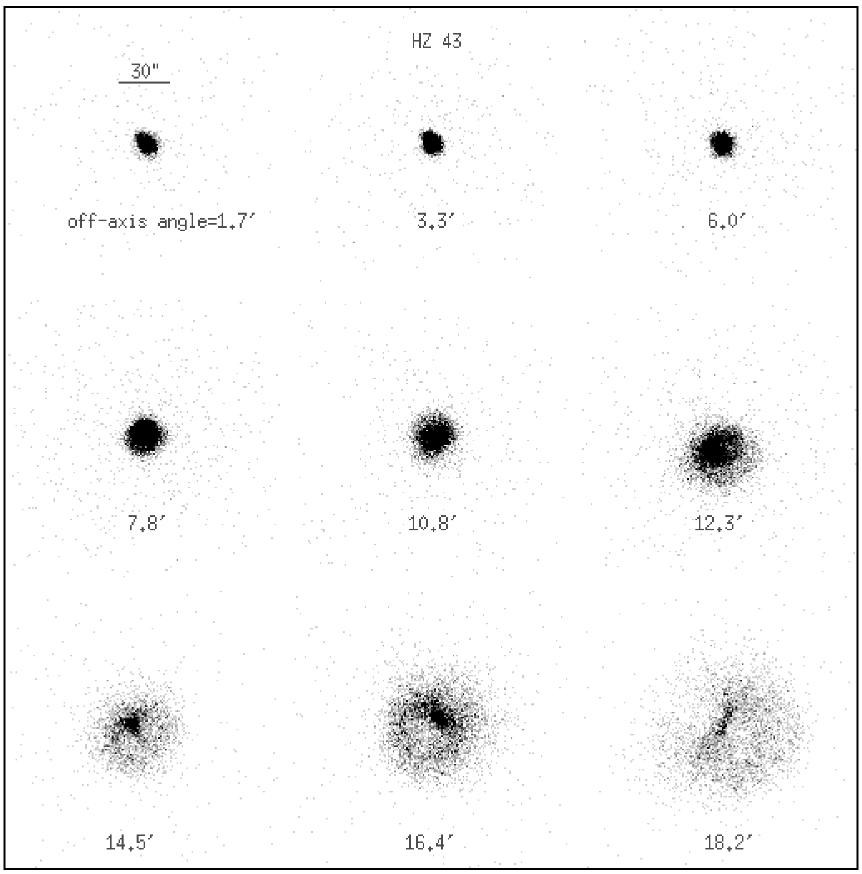

Fig. 7. HRI images of HZ43 at nine different angles off-axis.

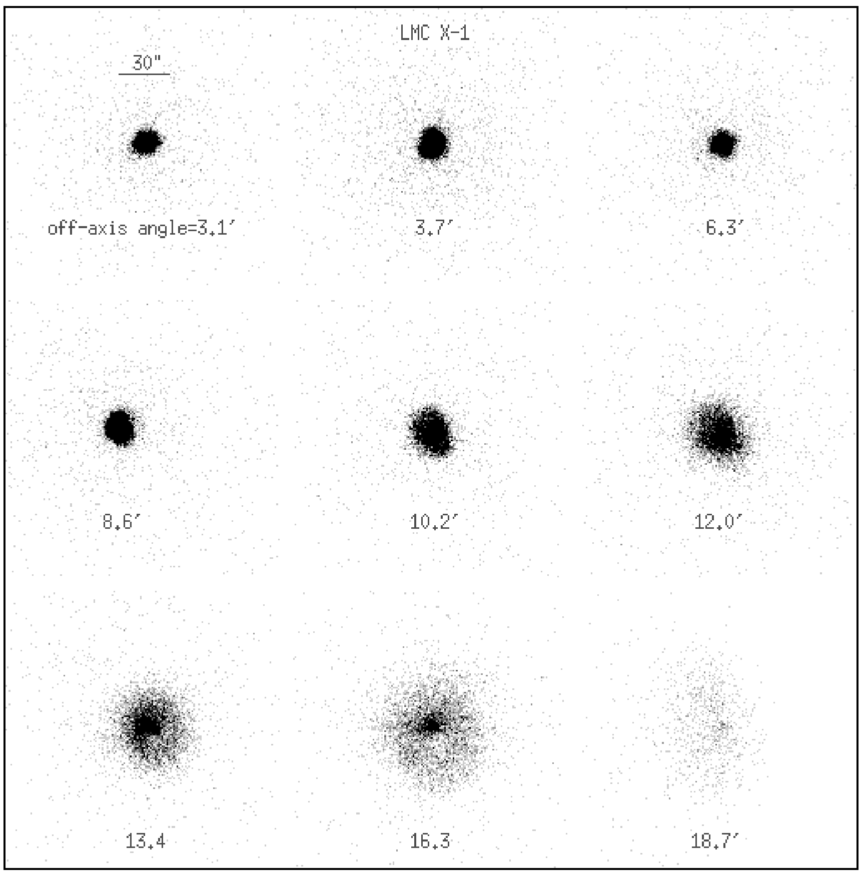

Fig. 8. HRI images of LMC X-1 at nine different angles off-axis.

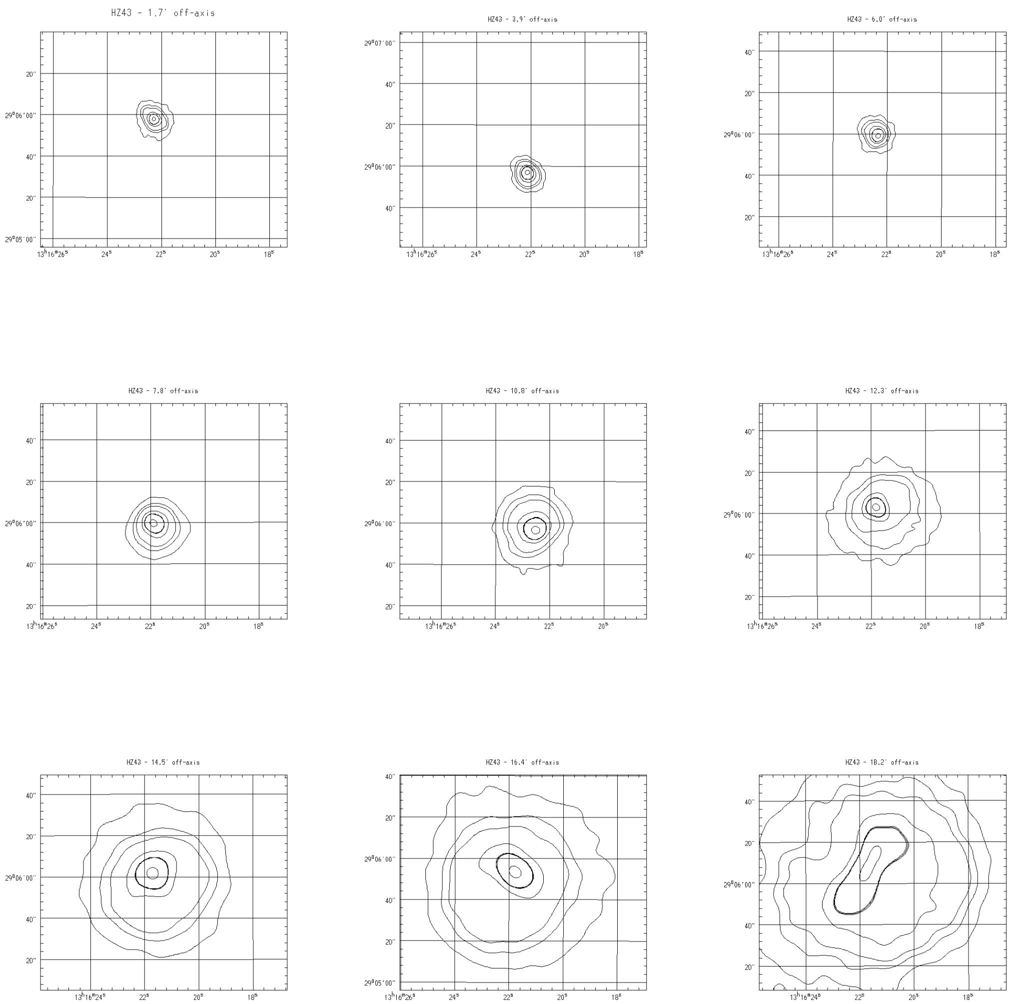

Fig. 9. Contour plots of the HZ43 images. The contours are at 1, 5, 10, 30, 50, and 90% of the peak value, with the 50% contour level shown in bold.

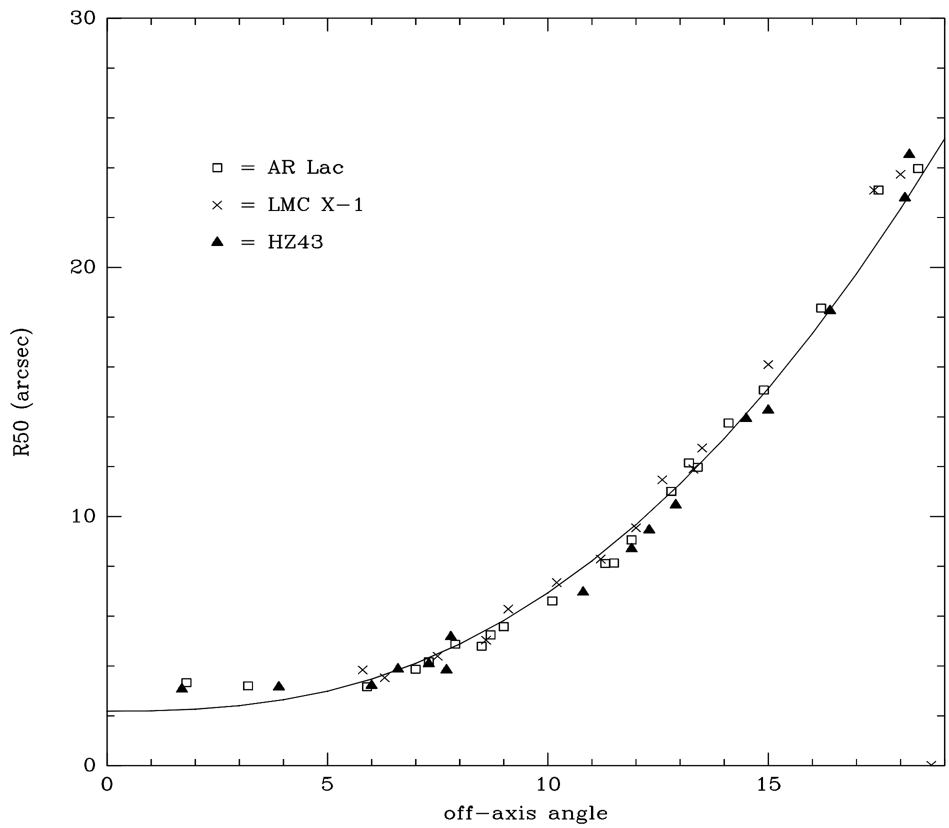

Fig. 10. The 50% power radius in images of HZ43, LMC X-1, and AR Lac as a function of angle off-axis. The parametric expression given in the text is also shown for comparison.

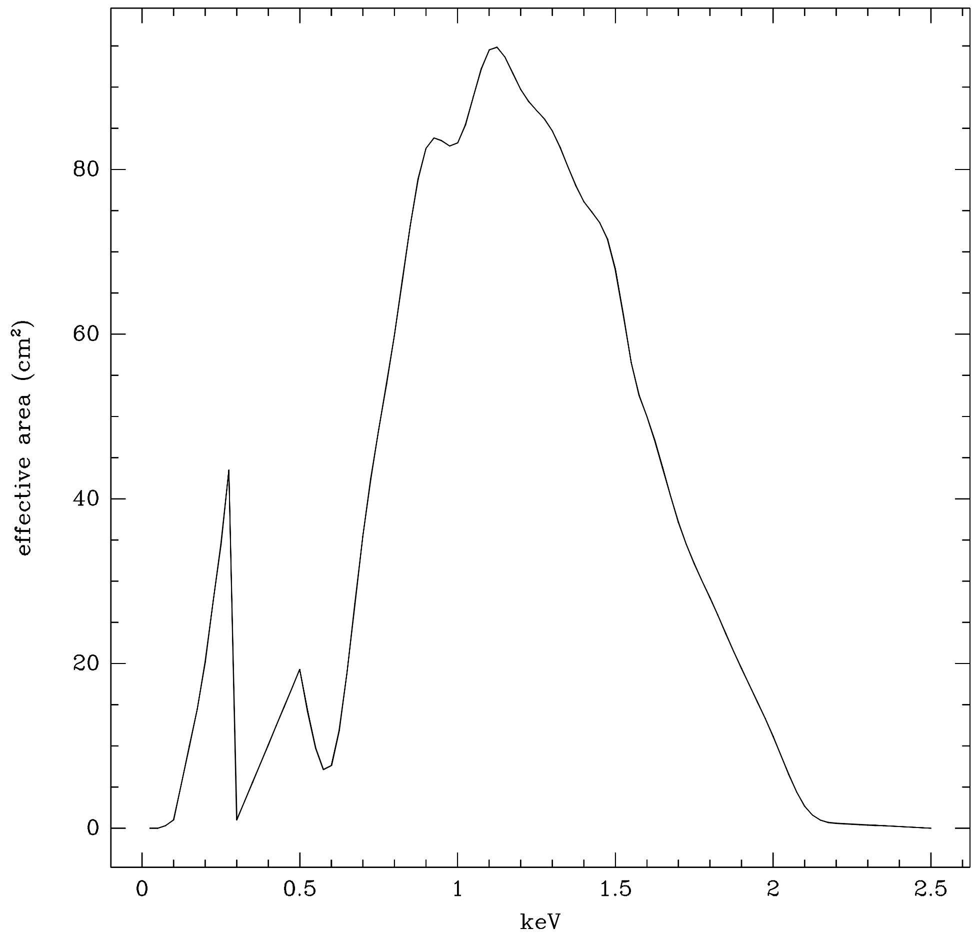

Fig. 11. The on-axis effective area of the XRT/HRI vs photon energy

Table 2
ROSAT XRT+HRI Effective Area

Energy (keV)	Lambda (Å)	Effective Area (cm^2)	Energy (keV)	Lambda (Å)	Effective Area (cm^2)
0.10	124.0	1.0	1.10	11.3	94.5
0.20	62.0	20.2	1.20	10.3	89.7
0.28	44.3	43.5	1.30	9.5	84.7
0.28	44.1	0.0	1.40	8.9	76.1
0.30	41.3	1.0	1.50	8.3	56.5
0.40	31.0	10.6	1.60	7.8	50.0
0.50	24.8	19.3	1.70	7.3	37.2
0.60	20.7	7.6	1.80	6.9	28.0
0.63	19.7	11.9	1.90	6.5	19.4
0.70	17.7	35.5	2.00	6.2	11.2
0.80	15.5	59.9	2.10	5.9	2.7
0.90	13.8	82.6	2.20	5.6	0.6
1.00	12.4	83.2	2.30	5.4	0.4
			3.40	5.2	0.2

3.3.2. Off-axis Effective Area

The XRT effective area varies smoothly with off-axis angle and energy. Figure 12 shows the XRT vignetting function (normalized to unity on-axis) for a range of photon energies. Vignetting is less than a 10% effect within $10'$ at all energies of interest. The vignetting function at 1.0 keV is well fit with the following parametric representation:

$$V(\Theta) = 1.00 - 1.49 \times 10^{-3}\Theta - 3.07 \times 10^{-4}\Theta^2$$

where Θ is in units of arc minutes.

The spatial uniformity of the HRI quantum efficiency was measured six months before launch in a series of flat field tests at three energies: 0.28, 0.93, and 1.49 keV. The quantum efficiency of the HRI varies by less than 10% over the detector and is nearly energy independent. Figure 13 is a representative contour plot of the spatial variation in the quantum efficiency of the HRI.

3.3.3. Long-term stability

It appears that the effective area has not varied significantly since launch. Observations of the sources HZ43, Vega, A2256, and N132D at several epochs yield non-varying count rates (Table 3).

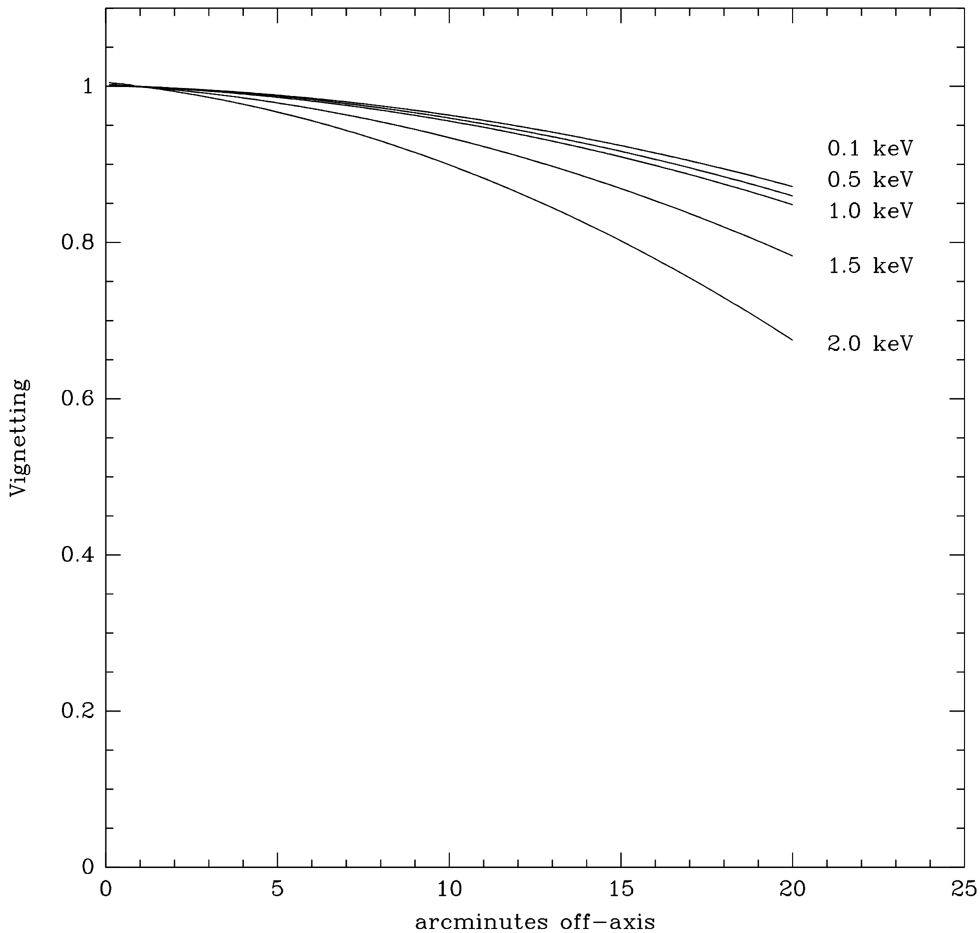

Fig. 12. The vignetting function of the XRT at 5 photon energies in the HRI field of view. The vignetting function is normalized to unity on-axis.

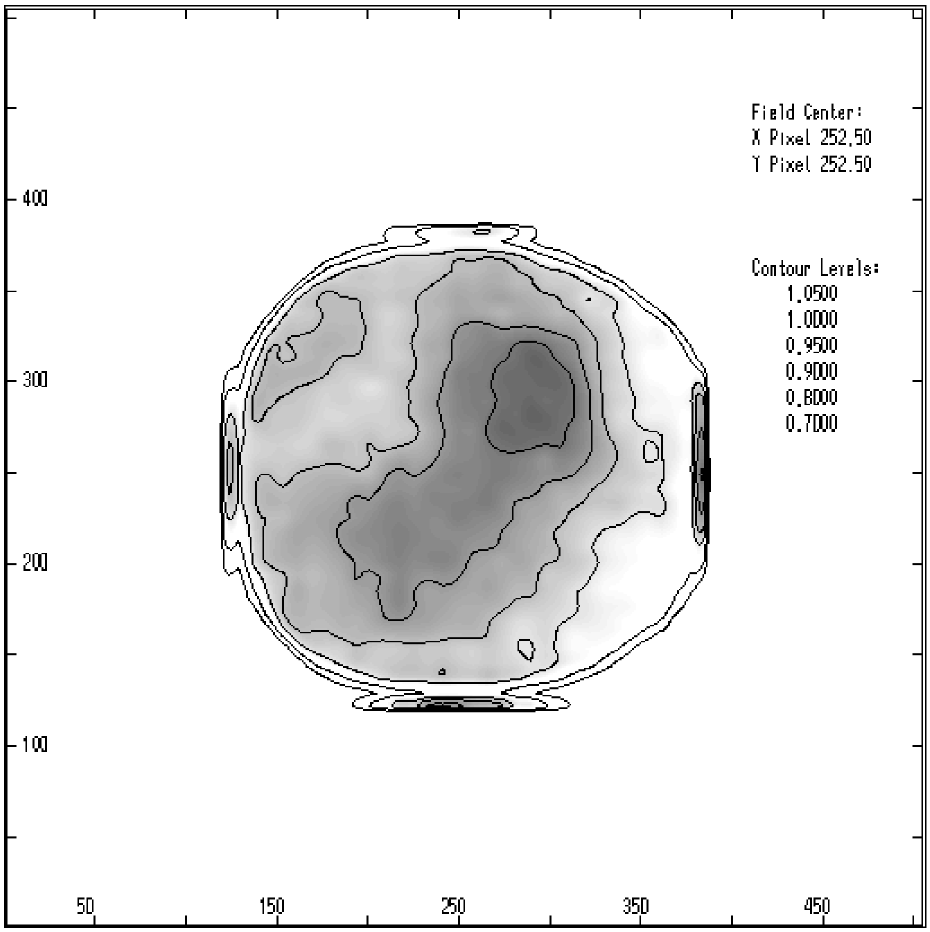

Fig. 13. Contours of the HRI QE map used by the on-line processing (SASS). The image has been blocked by a factor of 16 yielding 8″ pixels. The QE map shown in this figure was generated by combining ground based flat field measurements at C(0.28 keV), Cu(0.93 keV), and Al(1.49 keV) in the correct proportions for a power law spectrum with an energy index of -1. The composite image was then smoothed with a 32″ gaussian producing statistical errors of 1%. The QE is normalized to unity on-axis and the contours are at 0.7, 0.8, 0.9, 0.95, 1.0, 1.05 and decrease outward. Note that the QE of the HRI varies by less than 10% over most of the field of view.

Table 3
HRI QE Stability

Source	Date of Observation	Count Rate (counts s^{-1})
A2256	July 1, 1990	0.61 ± 0.01
	August 3, 1992	0.62 ± 0.01
HZ43	July 2, 1990	12.3 ± 0.2
	December 11, 1991	12.0 ± 0.2
	June 9, 1992	11.91 ± 0.04
Vega	March 20, 1991	0.10 ± 0.01
	March 21, 1992	0.11 ± 0.01
	Sept 18, 1992	0.10 ± 0.01
	April 15, 1995	0.11 ± 0.01
N132D	1990 July 3	4.43 ± 0.09
	1990 July 4	4.50 ± 0.13
	1991 February 9	4.54 ± 0.01
	1991 December 11	4.49 ± 0.09
	1992 June 10	4.40 ± 0.04
	1992 August 3	4.21 ± 0.05
	1992 September 17	4.57 ± 0.05
	1993 April 17	4.46 ± 0.04
	1994 January 10	4.40 ± 0.04
	1994 March 10	4.39 ± 0.06
	1994 June 15	4.56 ± 0.04
	1994 July 15	4.53 ± 0.05
	1994 August 15	4.54 ± 0.06
	1994 September 15	4.49 ± 0.06
	1995 February 11	4.40 ± 0.04
	1995 March 11	4.51 ± 0.04
	1995 October 20	4.54 ± 0.06
	1995 November 20	4.51 ± 0.04
	1996 January 20	4.59 ± 0.05
	1996 February 20	4.34 ± 0.04
	1996 April 20	4.23 ± 0.05
	1996 May 20	4.45 ± 0.07
	1996 June 20	4.10 ± 0.04
	1996 August 20	4.63 ± 0.05
	1996 September 20	4.43 ± 0.05
	1996 December 27	4.36 ± 0.05
	1997 March 5	4.30 ± 0.09
	1997 April 5	4.19 ± 0.04

Note: The count rate for A2256 is determined from the net emission within a $6'$ radius.

3.3.4. Source Count Rates

Table 4 shows measured HRI count rates for a sample of sources and compares these rates to that of the PSPC and the Einstein Observatory HRI and IPC.

Table 4
X-ray Count rates (counts s^{-1}) for different instruments

	Object	ROSAT HRI	*Einstein* HRI	ROSAT PSPC	*Einstein* IPC
	HZ43	12.0	3.6	100	3.8
v	AR Lac	0.65	0.69	7.4	1.3
v	Cyg X-2	72	27.8	180	NA
v	LMC X-1	3.8	1.3	10	10.55
v	LMC X-3	2.6	2.7	NA	NA
	Cas A	17	6.3	57	61
	Tycho	10.2	3.4	NA	22.3
	Kepler	5.4	1.7	NA	7.3
	E0102.2-72.2 (SMC SNR)	0.96	0.25	NA	0.79
	N132D	4.5	1.1	10.6	4.0
	A2256	0.62	NA	1.7	0.34

Notes: v - variable source, the count rate for A2256 is determined from the net emission within a $6'$ radius.

3.4. Background

The HRI in-orbit background is composed of several components:

a) The internal background is believed to come mainly from residual radioactivity in the MCP glass and the surrounding detector structure. This was measured on the ground with a rate of 1.5 counts s^{-1} over the entire device. This appears to be a stable component of the background and is uniform over the detector.

b) The X-ray background (XRB) contribution (comprised of both galactic and extragalactic components) varies across the sky, with a typical value in the ROSAT energy band of 1.0 count s^{-1}, over the detector.

c) The externally induced background from charged particles, earth scattered solar radiation, and auroral photons. On average, the externally induced background rates are higher for ROSAT than for Einstein due to the higher inclination and altitude of the orbit. The external background rates vary considerably during an orbit and also from orbit to orbit, with a minimum of 1 count s^{-1} up to about 10 counts s^{-1}, at which point the HRI high voltage is reduced to protect the detector from overload.

Figure 14 shows the variation in the background rate during an HRI observation of the North Ecliptic Pole (NEP). The lowest rates occur when the satellite is crossing the geomagnetic equator and the highest rates occur at the northern and southern extremities of the orbit. In many cases the HRI high voltage needs to be reduced in these regions to protect the detector from overload. Table 5 summarizes the average in-orbit values (and ranges) of all the background components.

Table 5: HRI Background Rates

Internal	1.5 (1.0-2.0)	counts s^{-1}
External	3.0 (1.0-10)	counts s^{-1}
XRB	1.0 (0.5-2.0)	counts s^{-1}
Total	5.5 (2.5-14)	counts s^{-1}
	7.8×10^{-1}	counts s^{-1} cm^{-2}
	3.8×10^{-3}	counts s^{-1} $arcmin^{-2}$
	1.1×10^{-6}	counts s^{-1} $arcsec^{-2}$

Figure 15 compares the pulse height analyzer (PHA) distribution of the background in the NEP observation during low background intervals (count rate < 5.0 counts s^{-1}; dominated by detector noise and the XRB) and high background intervals (count rate $>$ 5.0 counts s^{-1}; dominated by externally induced background events). Even though the background is dominated by different particles during these intervals, the spectra are consistent given the very modest energy resolution of the HRI. The background rate is the greatest in the lowest PHA channels since radioactive decay in the MCP glass and charged particles can produce electrons anywhere within the MCPs. These electrons are accelerated through through a smaller potential difference than electrons produced near the entrance of the MCPs. The background in PHA channels < 10 is very uniform across the detector. The background in PHA channels > 10 is enhanced beyond $15'$ off-axis due to the greater gain in the detector (see §3.5).

Also shown in Figure 15 is the PHA distribution in an HRI observation of AR Lac. Notice that the AR Lac spectrum is much more strongly peaked than the background spectrum. Most of the AR Lac source photons fall between PHA channels 3 and 7. In general, to obtain maximum sensitivity for detecting point sources or for analyzing low-surface brightness extended objects, the user is advised to screen out the highest background intervals and only examine PHA channels between approximately 3 and 8, inclusive. The optimum range of PHA channels depends on the source, the source position on the detector, and the date of observation. The user is advised to compare the source and background spectra for each observation to determine which channels should be screened out.

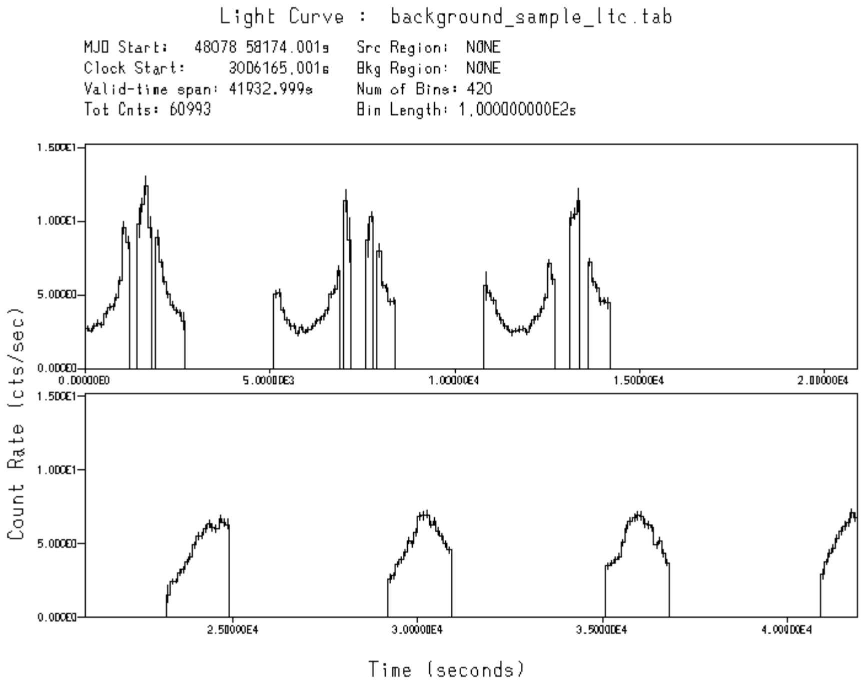

Fig. 14. The background rate over the entire HRI field in a portion of the 40 ks observation of the NEP

3.5. Spectral Response

The HRI, with its CsI-coated MCPs, was found during ground testing to possess a crude spectral sensitivity which has been verified with in-flight data. Funds to investigate this capability were recently provided by the NASA Astrophysics Data Program(ADP). In this section, we summarize the spectral attributes of the HRI detector and then describe the preliminary results of the ADP investigation to date. This project is still on-going, hence efforts to derive quantitative spectral results from HRI data must entail careful analysis on the part of individual investigators.

Figure 16 shows the PHA distribution from ground-based measurements at 7 energies, and Table 6 lists the mean PHA channel at each energy. Note that there is a systematic increase in the mean pulse height channel with increasing photon energy except for the Si line (the Si measurement may have been affected by the presence of Si in the glass in the microchannel plates). Table 6 shows that the mean PHA varies by approximately 2 channels over the energy range of the *ROSAT* mirror.

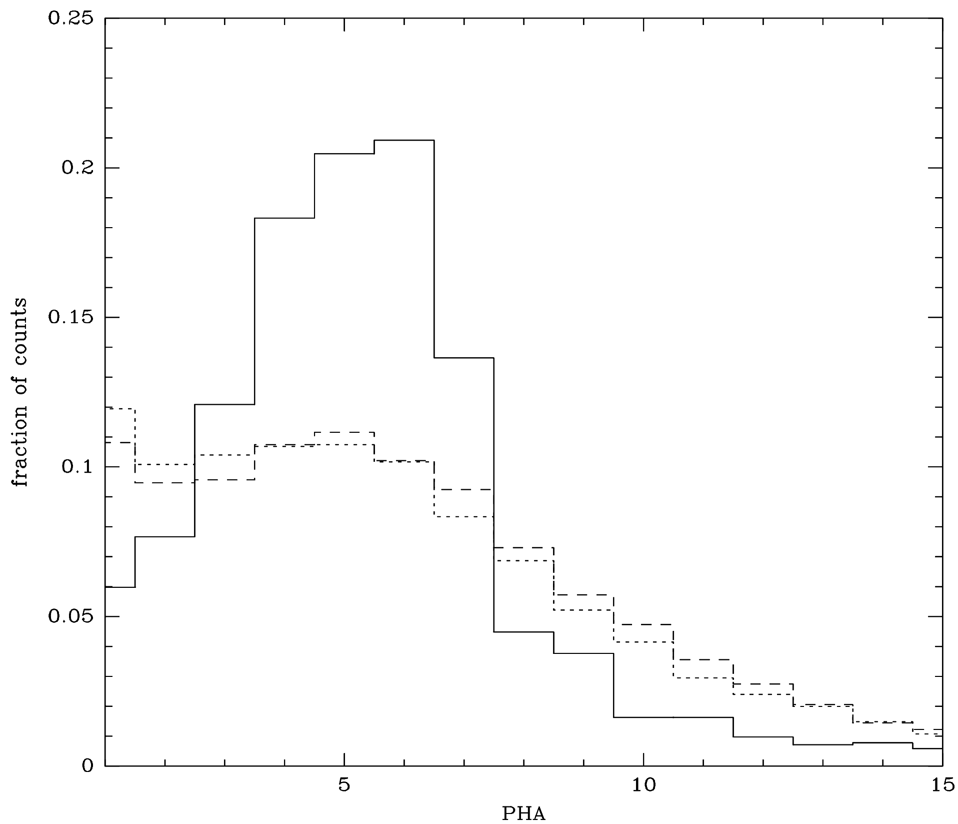

Fig. 15. The PHA distribution of the HRI background during high background intervals (dashed curve), low background intervals (dotted curve), and AR Lac (solid curve)

Table 6: Mean PHA from ground-based measurements

X-ray target	mean PHA
B (0.18 keV)	3.30
C (0.28 keV)	3.96
O (0.53 keV)	3.99
Fe (0.71 keV)	4.15
Cu (0.93 keV)	4.58
Al (1.49 keV)	5.44
Si (1.74 keV)	4.82

3.5.1. Spatial Gain Variations

It was found from the ground based flat-field measurements that the gain of the HRI varies spatially across the detector. Figure 17 is a contour map of the mean pulse height channel for the Cu-K (0.93 keV) flat field data averaged over a spatial scale of about $1'$. The mean pulse height channel increases from 4 near the center of the detector to approximately 7 near the edge. However, within $5'$ of the optical axis, the gain only varies by 10%. The spatial variation in the gain is similar at all photon energies. In Figure 18 we show the computed average channel for HZ43 and AR Lac plotted against the expected value at that position on the detector from the Cu gain map.

The RSDC at SAO has produced FITS versions of the gain maps such as that shown in Figure 17; available via anonftp: sao-ftp.harvard.edu (cd pub/rosat/calfiles) and on legacy. These maps have a scale of $8''$/pix and are thus useful (when rolled to match an observation) for determining the relative gains of features. Users should be mindful that (a) The gain maps were made from ground calibrations before launch, and therefore do not represent accurate values for any given date during the mission (see the next section); (b) the normal satellite's wobble will mean that any X-ray feature will actually experience the gains from somewhat different areas of the detector; and (c) observations taken over intervals of more than a few days will often have a range of roll angles (section 3.5.3).

3.5.2. Temporal Gain Variations

The pulse height distribution for celestial sources and the UV calibration lamp have displayed a systematic change with time. The peak and mean pulse height channel have shifted to lower values. Figure 19 shows the pulse height distribution of three HRI observations of N132D. Notice that the peak (and mean) in the pulse height distribution had decreased by 2 channels before the high voltage increase, a change comparable to the difference between the response of the HRI to the Al-Kα line (1.49 keV) and B-Kα line (0.18 keV) measured during the ground based tests. Figure 20 displays the HRI gain history using multiple on-axis observations of N132D and a selected subregion from the UV cal lamp data.

We have used the in-orbit bright earth data to monitor the gain map, and determine whether the spatial structure observed during ground-based tests has varied during the mission. By composing gain maps of the bright earth data we find that the decrease in the HRI gain evident in Figure 19 is uniform across the detector.

3.5.3. Corrections for Spatial and Temporal Gain

In this section, we describe our attempts to correct the ground-based response matrix for spatial and temporal gain variations described in the previous section. We used Bright Earth data to monitor the gain variation both as a function of position on the detector and time during the mission (see above). The Bright Earth data are dominated by scattered solar

X-ray emission, primarily an atomic oxygen line at 0.525 keV, thus effectively providing a monochromatic flat-field. We have extracted the BE HRI map for 32 epochs throughout the first 5 years of the mission. Each map consists of a 32×32 array; 128 arcsec/pixel; with the pixel size determined by a compromise between the spatial resolution and the S/N. We fitted all 33,000 spectra with a Pearson function (Fraser 1992, file "spec_resp_zero.tex", available on GSFC anonymous ftp node legacy.gsfc.nasa.gov, in sub-directory "/rosat/doc/hri") and an additional exponential component at higher channels. This data set provides the gain appropriate for a given observation. In addition, we have written software to recover the detector position for a given source by de-applying the aspect solution. This allows the user to determine the range of gain states the source experienced as it is wobbled over the detector. This information allows a response matrix to be constructed which is weighted by the time spent in any given gain state.

3.5.4. Spectral Response Matrix

Using the ground-based data (see Figure 16) we constructed a spectral redistribution matrix for the HRI. The matrix is in OGIP FITS format, and can be used in XSPEC. We then fit the pulse height distributions of archival observations of HZ43 obtained between July 1990 and June 1992 and several observations of AR Lac. PSPC spectra of HZ43 are well fit with an unabsorbed blackbody spectrum with a temperature of 0.02 keV ($\chi^2 = 27$ for 24 degrees of freedom). AR Lac PSPC data was fit by a Raymond-Smith plasma plus a powerlaw component (kT=0.87 and photon index 1.52). Table 7 lists the χ^2 values for selected observations with only the normalization treated as a free parameter. The minimum χ^2 values are extremely high because the instrument gain is different from the ground-based value.

To determine how well the ground-based response matrix can be corrected for the effect of spatial and temporal gain variations we repeated the fits to HZ43 and AR Lac, allowing the response matrix gain to change. This procedure involved fixing the input model source spectrum and allowing the response matrix to shift in channel space until a best fit was obtained (χ^2 was minimized; see Figure 21) The model normalization was also allowed to vary. These results are also shown in Table 7. Clearly, the fits are much improved. Figure 22 shows the response matrix shift (in channels) required to give a best fit plotted against the PHA maximum of the BE data at the time and position of the observation. There is a tight correlation between these two quantities, indicating that the BE data can be used to predict a response matrix gain shift. There is increasing scatter above a BE PHA maximum of ~ 5. These points are all from observations $> 8'$ offaxis, where the redistribution matrix changes. To obtain best results, only sources within $8'$ of the detector center should be used.

Work is in progress to provide these spectral capabilities to the community. Current plans involve a delivery to HEASARC by mid 1997.

Table 7

Spectral Fitting Results for HZ43

sequence	date	off-axis angle (arcmin)	χ^2 ground-based	χ^2 shifted
110196	7/2/90	1.7	247.3 (41.2)	4.420 (0.74)
110198	7/2/90	3.9	329.5 (54.9)	13.46 (2.24)
141809	12/11/91	1.3	28.94 (4.82)	3.99 (0.66)
110207B	03/07/90	10.3	302.1 (50.3)	9.15 (1.52)
110207A	03/07/90	10.3	1250 (208.3)	145.2 (24.2)

Note: A comparison of χ^2 values obtain by fitting selected HZ43 observations with the ground-based response matrix (column 4) and the response matrix shifted in channel space (column 5). Channels 4-10 were included in the fit, giving 6 degrees of freedom. The reduced χ^2 is shown in parentheses. The best fit is improved in all cases. The fit is still unacceptable more than $\sim 8'$ off-axis.

3.5.5. Hardness Ratios

While it is difficult to obtain quantitative spectral information from the HRI (i.e., temperatures or power-law indices), it is possible to obtain qualitative information on a scale of a few arcminutes using hardness (or softness) ratios. Wilson et al. (1992, Ap.J. Lett., 391, L75) showed that the extended emission in NGC1068 is harder than the nuclear component using a softness ratio defined by the channels [1:5]/[6:11]. Since the HRI gain varies temporally and spatially, the user may want to define the PHA boundaries on a case by case basis. For example, in the two observations of N132D shown in Figure 19, the fraction of the total counts in PHA channels 6-11 decreased from 40% to 10%.

3.6. UV Response

The preflight prediction of the detector UV response was underestimated. Vega (V = 0.03, A0 V, distance= 8.1 pc), a star relatively bright in the UV, gives a count rate of 0.10 counts s^{-1} (7 times that of the Einstein HRI), and beta Car (V = 1.68, A0 III, distance=26 pc) gives a count rate of 0.006 counts s^{-1}.

At the 1996 May HEAD meeting in San Diego CA, S. Murray presented the results of some testing done on UV filters in conjunction with AXAF work. UV filters similar to those flown on ROSAT were also tested.

Whereas the conventional wisdom held that the primary UV "leak" for the ROSAT HRI occurred in the band 1500 to 1900 angstroms, there were at least two problems with that explanation (Silverman, Harris, and Kearns, 1996):

a) The predicted UV-leak count rate for Vega was about a factor of 100 lower than measured; and

b) The PHA distribution of Vega was significantly different (i.e. peaked at a smaller PHA) than that for the UV calibration lamp (primarily an emission line of mercury at 1830 angstroms). This can be seen by comparing figures 23 and 25.

Murray and his colleagues found a number of transmission bands above 2300 angstroms, and conclude that having the aluminium coating on both faces of a filter creates a "lexan sandwich" which then exhibits the behavior of an interference filter.

It is not possible to make precise quantitative predictions because there is no laboratory filter exactly identical to the ROSAT flight models (however, see Zombeck et al. 1997, in preparation). Several ROSAT filters were manufactured and one set has been held in storage at SAO. However, there is significant variation in the filter thickness and coating thickness compared with the actual flight article. There is also a possible aging effect on the Aluminum coating - oxidation - that differs between the flight filter and the laboratory sample.

We can however conclude that there is excess transmission in the region from 2000-4000 angstroms and this may be responsible for the high count rate of Vega (0.1 counts s^{-1}). There is great uncertainty in the CsI photocathode response in the UV (from 1000-4000A) which makes the picture even more confused, but it is reasonable to ascribe the "softer" PHA distribution to the fact that softer photons (than the UV calibration lamp) cause the leak. Even if we get the filter completely right, there is no direct measurement of the photocathode.

3.7. Event Timing

Each event detected with the HRI is time tagged with a precision of 61 μs relative to the ROSAT spacecraft clock. The processing time for determining the position of an event is dependent upon the event location between the readout taps in the crossed grid charge detector and varies from 0.36 to 1.35 ms. For an event rate of 100 counts s^{-1}, the dead time losses will vary from 4 to 15 percent. The standard dead time correction formula can be used: $n_t = n(1 + n\rho)$ where n_t is the

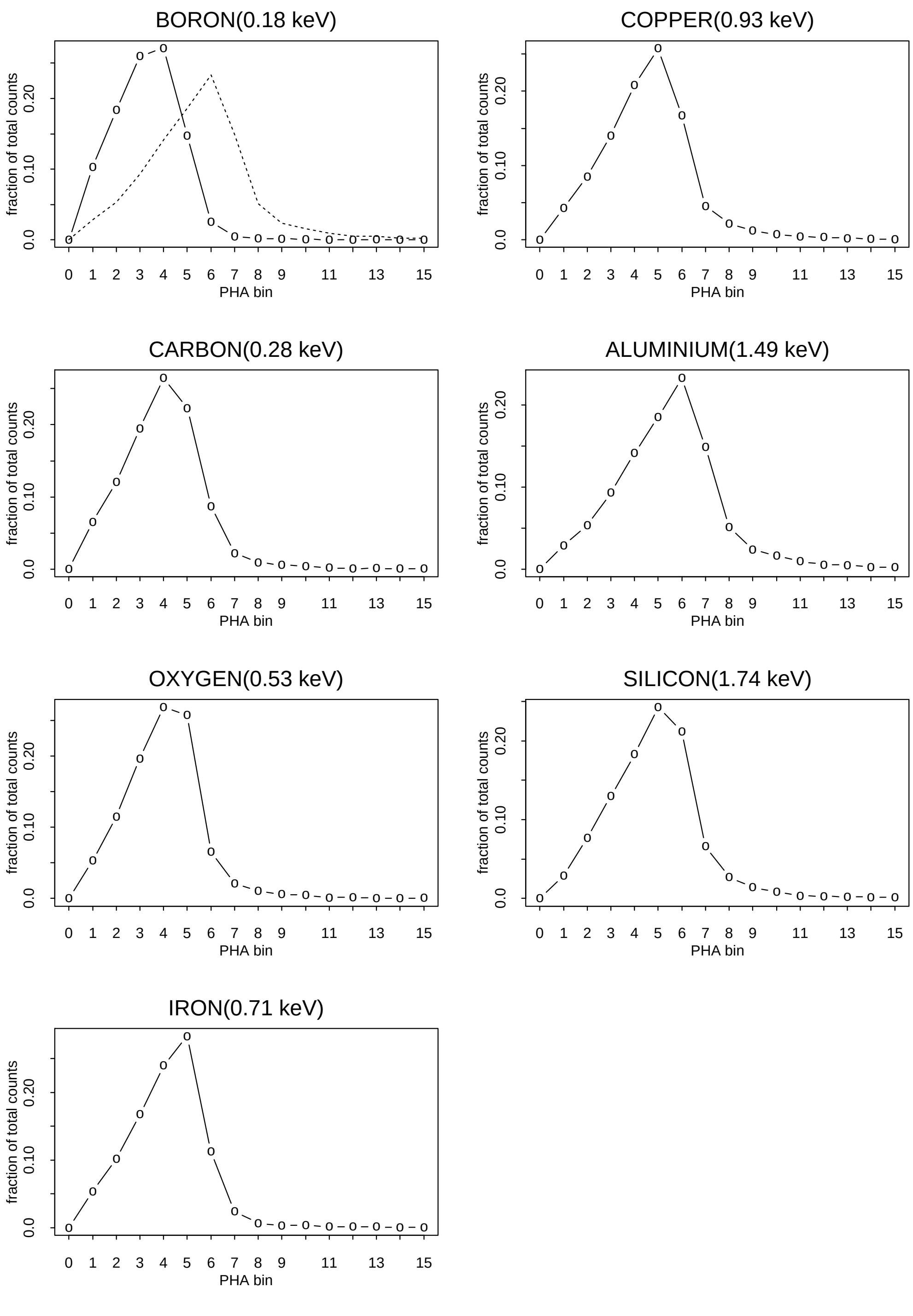

Fig. 16. The pulse height distribution from ground-based measurements at 7 energies within a $1' \times 5'$ strip centered on the detector The dashed curve in the Boron panel is the PHA distribution of the Al data, and is included to show the full spectral range.

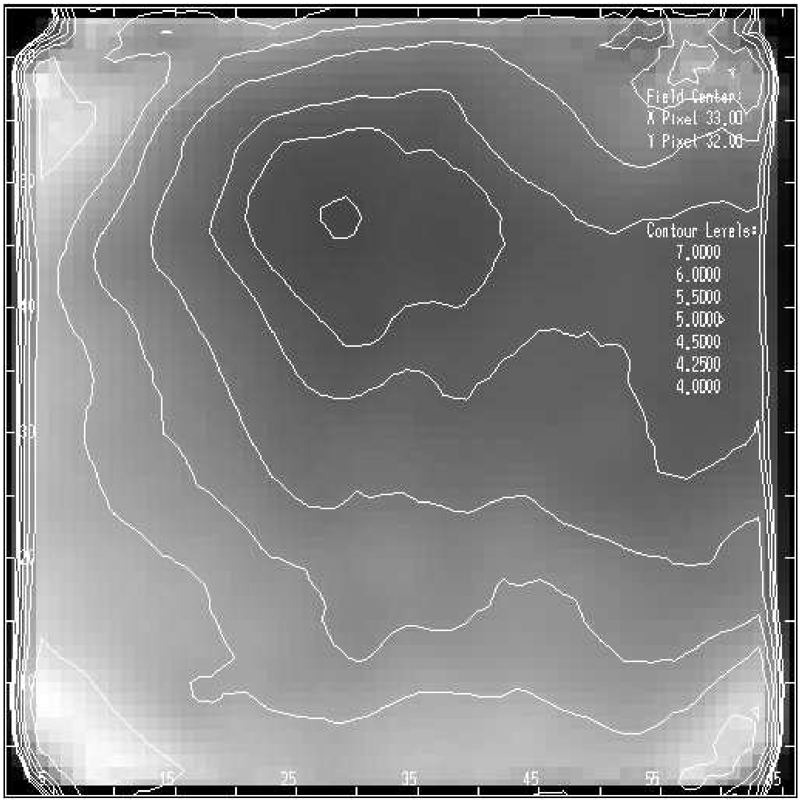

Fig. 17. The spatial variation in the centroid of the pulse height distribution in the ground based Cu(0.93 keV) flat field image. The image was first blocked by a factor of 64, producing $32''$ pixels with 1% statistical errors. The contours are at PHA values of 4.0, 4.25, 4.5, 5.0, 5.5, 6.0, 7.0 and increase outward.

true rate, n is the observed rate, and ρ is the dead time per event. The dead time varies linearly with position, but since source photons will be recorded over a distribution of fine positions due to spacecraft motion and the point spread function of the telescope, there is no single value of dead time for a particular source observation. As a first approximation, it is possible to use a typical value of $\rho = 0.85$ ms.

A separate scalar on the HRI counts preprocessed events with a dead time of only 30 μs. The contents of this scalar are entered into the telemetry once each second as secondary science. Thus if the HRI is observing a bright source, the intensity as derived from the processed events in the image can be corrected for the dead time using the data rates determined from the secondary science scalar.

3.8. High Voltage Increase

On June 21, 1994 at 8:59 GMT, the HRI high voltage was increased from level 12 to 13 in order to approximately recover the detector's original PHA distribution. Figure 24 shows an observation of the on-board UV calibration lamp taken during the HV increase. It exhibits an increase of 4% in the calibration lamp count rate, indicating the HV level change has approximately recovered the original UV sensitivity. In figure 25 the PHA distributions before and after the increase are compared with an observation taken shortly after launch, showing that the mean PHA has recovered to within 0.5 channels of the original. See also Figures 19 and 20.

The date and time given above for the change of HV from step 12 to 13 should not be used "blindly" because step 12 was commanded shortly afterwards by the inadvertent use of a standard

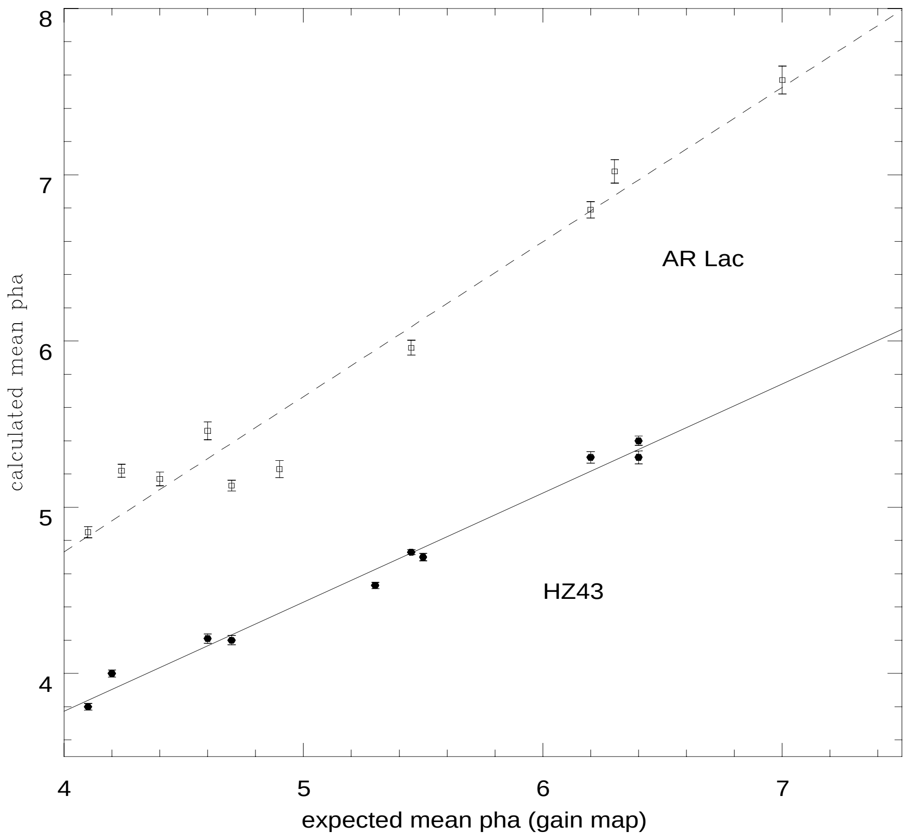

Fig. 18. PCV phase observations of HZ43 and AR Lac were taken at many positions on the detector surface. The observed mean PHA of the calibration source measurements are plotted with errors against the expected mean PHA from the ground based measurements of copper (0.93 keV). The line represents the best least squares fit of the data points.

parameter file. Lacking precise archival records, we recommend that the user examine the temporal status indicator record for any observation taken in June and early July of 1994 if he needs to know the HV setting. In figure 20, notice the "overlap" of coverage during this period, with data at both high voltage steps for N132D.

While turning the HRI back into the focus of the ROSAT XRT on March 3, 1997 (after the PSPC intermezzo), the initial high voltage setting (i.e. that used at the beginning of the mission, step 12) was inadvertently re-initiated. The mistake was only recognized two months later and the HV was reset to step 13 (which has been used since 1994 Jun) on 1997 May 6 at 12:40 UT.

3.9. Hotspot appearance

3.9.1. General

At the end of the Wurzburg conference (circa 29 September 1995) Thomas Preibisch alerted MPE about a feature near the edge of the HRI field. Approximately two weeks later, many datasets were examined at MPE and 3 sequences which showed this effect were identified. SAO was notified on 16 October. and subsequently examined this sporadic feature. Many people at MPE, GSFC, and at SAO have contributed to this report.

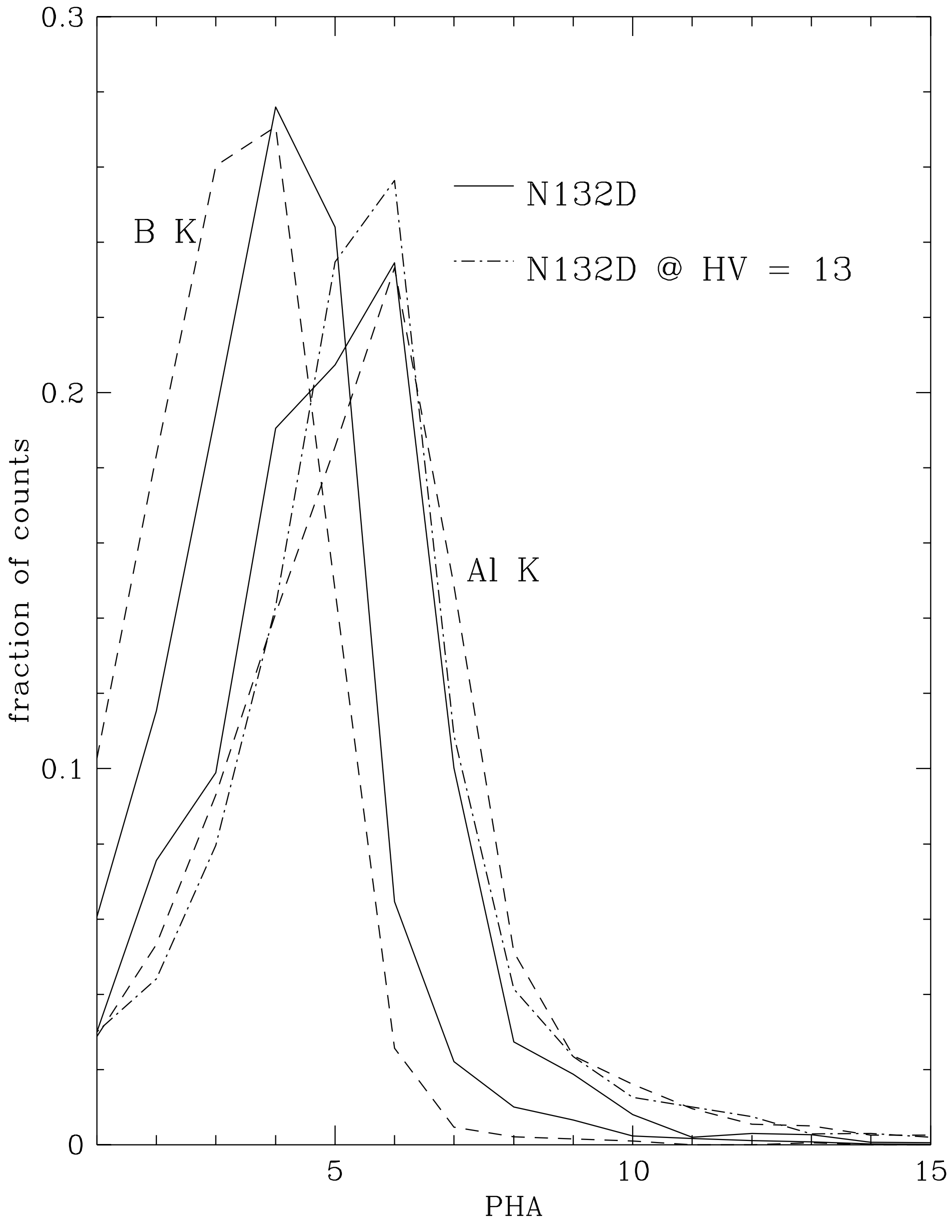

Fig. 19. The pulse height distribution in 3 HRI observations of N132D. The highest gain observation (solid line) was taken during the PCV phase, the lowest gain observation was taken in April 1993, and the observation shown in the dot-dash line was taken in July 1994, just after the HV increase. Also shown (dashed lines) are the pulse height distributions of the Al-K (1.49 keV) and B-K (0.18 keV) lines obtained during the ground based tests. Although the total count rate (in all PHA channels) has remained nearly constant (see Table 3), the earlier observations show a downward trend in the peak of the distribution. The latest observation shows that the HV increase has restored the peak to within 0.5 channels of the original.

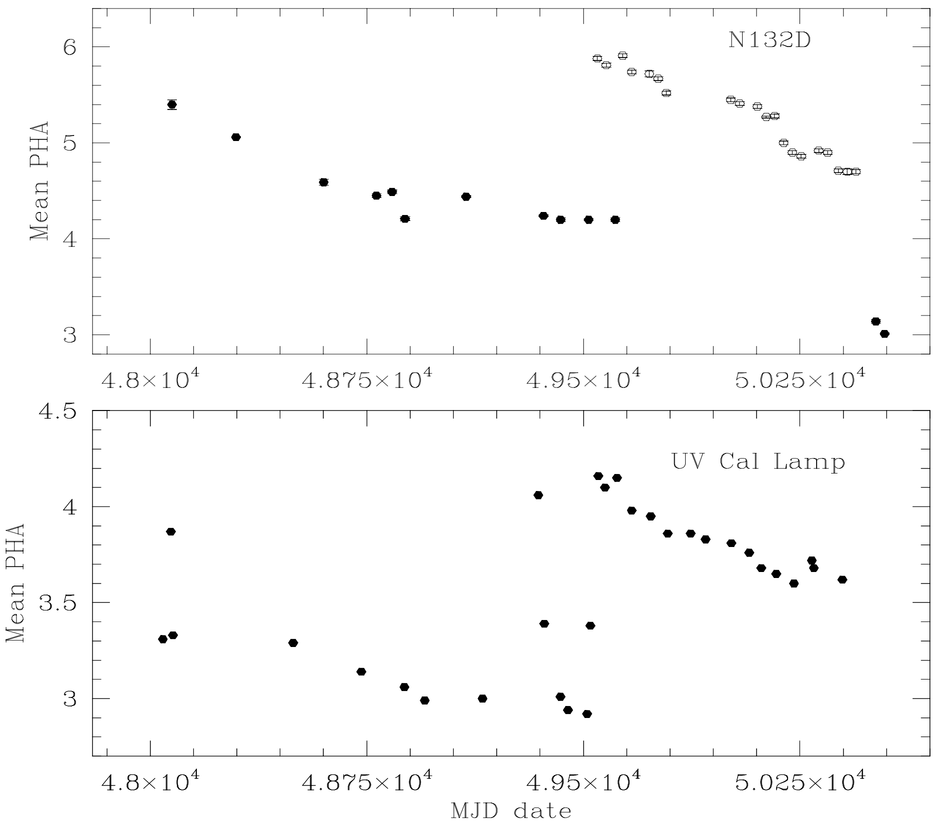

Fig. 20. The temporal status of the mean PHA channel of N132D and the UV calibration lamp (a small area near the center of the detector). The mean PHA is plotted for many observations starting in July 1990 through September 1996. For N132D, the open circles represent observations after the high voltage increase in June of 1994.

During the course of the ROSAT Results Archive visual inspection, J. Silverman discovered a second hotspot in a different corner of the detector.

Although the precise cause of HRI hotspots are not known, they are thought to be a defect in a single pore of the micro channel plate. Some of the hotspots discovered before launch were subsequently incorporated into the HRI "hotspot map" which is used in the SASS processing to reject all events happening at given locations.

The original hotspot (aka #1) and the second are similar in several respects but differ in their PHA distribution, their variability characteristics, and the length of time they have been active. Because of their respective locations, HS#1 appears as a radial streak (in a normally wobbled observation), often appearing to extend into the region where there are few or no background counts. HS#2 being in an adjacent corner, appears as a tangential streak.

While it is somewhat surprising that both hotspots appeared within a few months of each other after years of no occurrences, they seem to be isolated events; no additional hotspots have been found. Since they are both at the very edge of the detector and their intensity is small enough that they do not encroach on the telemetry limit, they have essentially no impact on the quality of the scientific returns of the HRI. Monitoring of both hotspots has been incorporated into the verification software running at SAO; MPE continues to watch current activity on quick look data from the satellite; and the ROSAT Results Archive quality checking serves as a backup monitor for

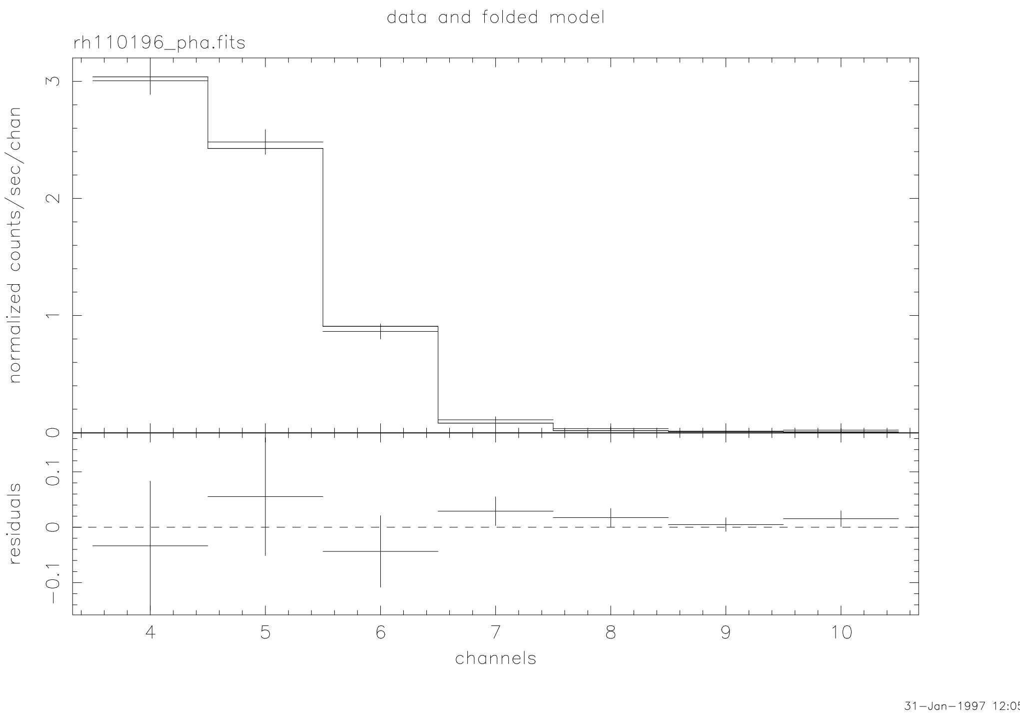

Fig. 21. The response matrix (solid line) convolved with a 0.02 keV blackbody shifted in channel space to give the best fit to an observation of HZ43 (crosses) in the top panel. The bottom panel displays the residuals.

any new occurrences.

3.9.2. Spatial

Both hotspots have quasi power law distributions (sigma = $1.4''$), with most of the counts falling within a circle of r=6 pixels. This size circle does not appear to be a function of time; even for short bursts, the spatial distribution is maintained.

	HOTSPOT #1	HOTSPOT #2
detector coordinates:	rawx = 440.5	rawx = 3636
	rawy = 484.5	rawy = 552

3.9.3. Temporal

For #1, an examination of light curves and plots of the KS test show that there are many intervals and obis when no activity is seen. #2 is quite different, being more steady (less "sparking" or

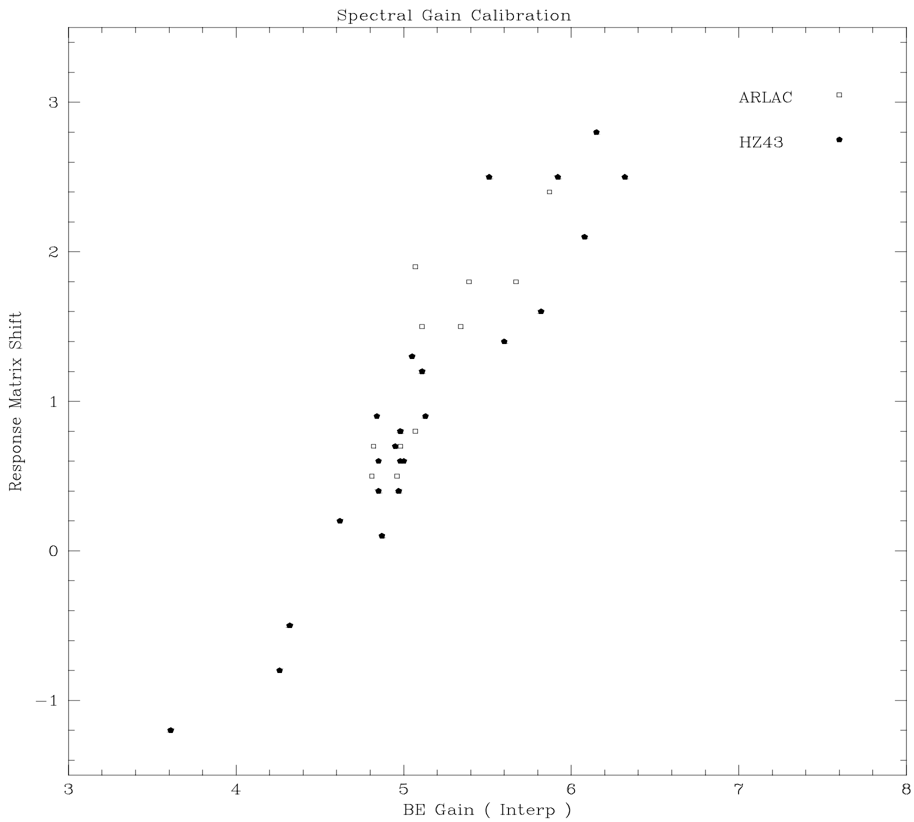

Fig. 22. Response matrix shift (in channels) required to give a best fit plotted against the PHA maximum of the Bright Earth data for observations of two standards, AR Lac and HZ43.

"flickering"). For both, the average count rate drops quickly as the length of the time bin is increased.

	HOTSPOT #1	HOTSPOT #2
First known occurrence	8Jul95/rh800694	mid-Mar95
Largest known c/s (1 s bins)	57(rh300399)	much less than #1
Largest known <c/s> for a seq:	0.76 (17.2 ks)	0.0177(28 ks)
Incidence of Detection (Jul-Sep 1995)	120 out of 240 seqs;	7/240

During 1996, the activity of both hotspots subsided to the extent that they are only detectable on rare occasions using their known location for precise measurements.

3.9.4. PHA

The PHA distribution differs for the two hotspots.

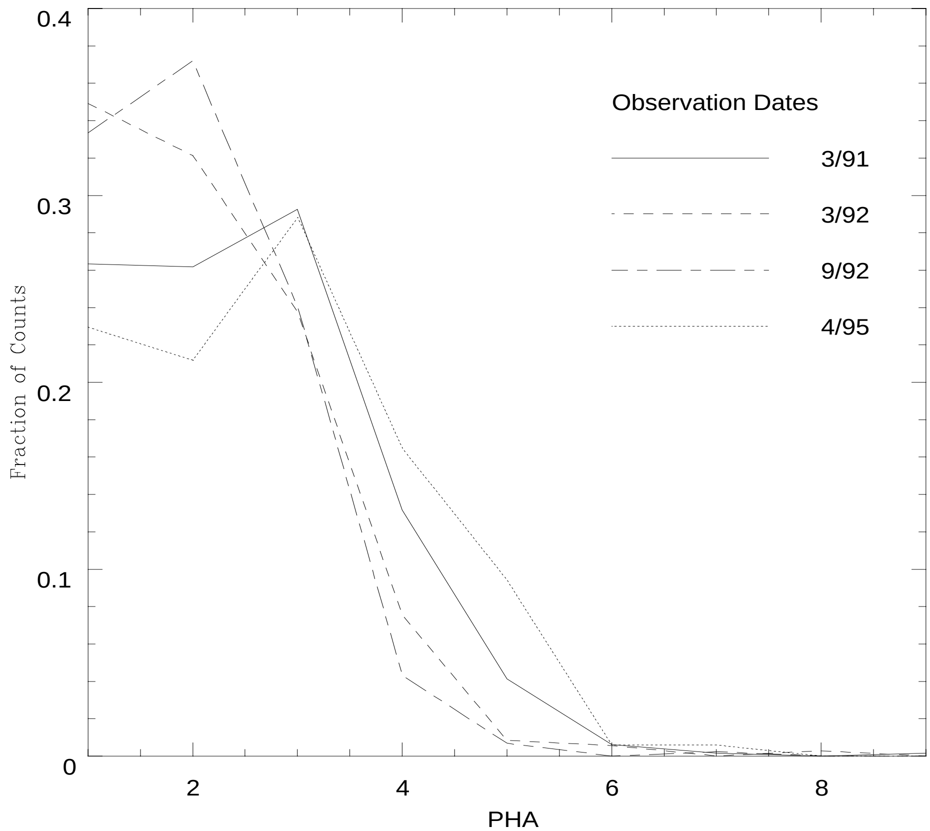

Fig. 23. The pulse height distribution in several HRI observations of Vega. While the peak in the pulse height distribution has continuously shifted downward during the mission, the total count rate (in all PHA channels) has remained nearly constant (see Table 3). The high voltage increase in July 1994 has temporarily restored the PHA distribution as evident in the data taken in April 1995.

HOTSPOT #1	HOTSPOT #2
85% in channel 1 15% in channel 2 <1% in channel 3	peaks in channel 1; then decreases with about 1/2 counts in channels 4-10.

3.9.5. Viewing and Deleting

To view the hotspot in PROS;

```
> xdisplay "rh123456n00.qp[key=(rawx,rawy][186:697,230:741]"
(change coordinates for HS#2)
OR > xexamine rh...qp[key=(rawx,rawy)]
```

To make a KS plot, in the xtiming package of PROS,

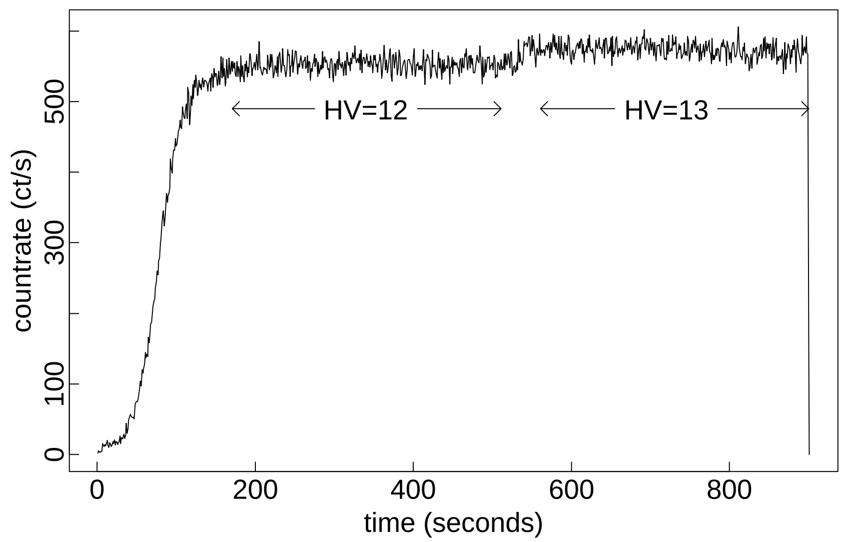

Fig. 24. UV calibration observation taken during the HV change, showing a 4% increase in count rate. The marked regions are those used in the following figure.

```
> timsort rh....qp[key=(rawx,rawy)]
region: box 441 485 20 20
> vartst

> ksplot
```

To obliterate the hotspot, use qpcopy with the same [key=...] as above and specify a region (box or circle) to be excluded.

To view the hotspot in MIDAS/EXSAS:

in EXSAS the following commands will produce "detector images (200x200)" with hotspot No.1 and No. 2 in the center with the maximum resolution:

```
bin/image XDET,YDET 1 pixel ,340,384,540,584   *events *hs1-area
bin/image XDET,YDET 1 pixel ,3536,452,3736,652 *events *hs2-area
```

4. Feasibility of observations

All guest investigators are asked to quantitatively discuss the feasibility of their proposed ROSAT observations. This section provides guidelines as to how to proceed with HRI observations.

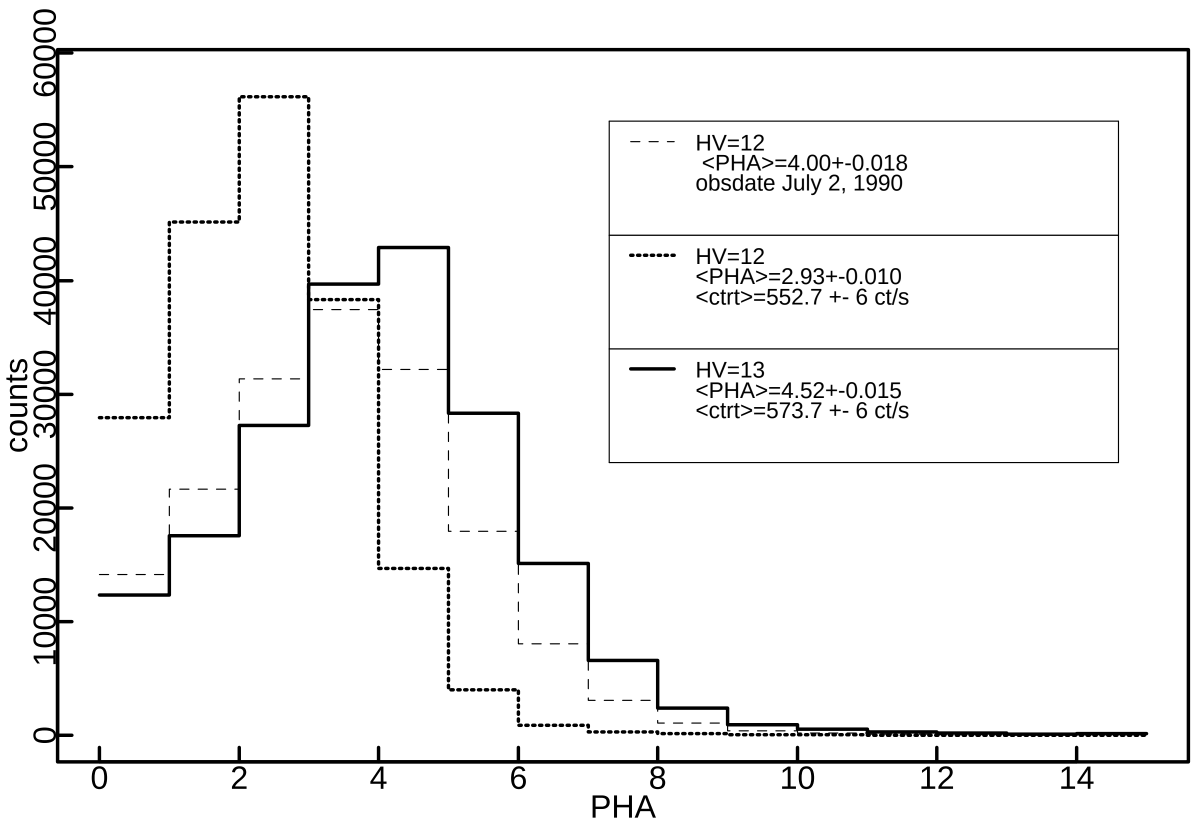

Fig. 25. Comparison of PHA distributions of UV calibration data taken shortly after launch (dashed line) with data taken immediately before and after the HV change, June 21, 1994. (Counts are normalized to equal obstimes.)

4.1. General Assumptions

In order to estimate the HRI response to a cosmic X-ray source, several performance characteristics of the combined HRI and ROSAT telescope are needed. In the sections that follow we provide estimates of minimum source count rate detection and expected count rates from sources. The assumptions that were used in providing these estimates are:

– The effective area shown in Figure 7 and listed in Table 3 (Table 11.1 of Appendix F) is the product of the XRT area and the HRI quantum efficiency.
– The HRI point source detection cell size is chosen so that 50 percent of the source photons fall within the detection cell. Hence the cell size must be matched to the XRT point spread function, the HRI detector resolution, and the aspect uncertainty (the latter currently being the largest factor in this choice).
– The HRI background rate is discussed above in section 3.4. For the present purposes, the X-ray background was computed from the spectrum shown in Figure 11.2 of Appendix F, which is a compilation of Wisconsin and LLL measurements (Ap.J. 193, L133; Ap.J., 172, L67) of the diffuse galactic background, and an extrapolation of a power law fit to the

extragalactic background. In estimating the HRI count rate we integrate this spectrum over the total effective area of the XRT/HRI. Note that the UV/Ion Filter and electrostatic shield greatly reduce the HRI sensitivity at low energies and that there is a major dip in effective area at the carbon edge. It should also be noted that the galactic component of the X-ray background varies with the viewing direction. We have taken a conservative estimate of the galactic background in the sense that we use the high emission estimates in calculating the HRI count rates. In some cases the HRI background count rates due to galactic emission may be up to a factor of 5 lower than the value of 1.0 count s^{-1} used here and section 11 of Appendix F.

None of these assumptions is absolutely correct, but they provide a typical description of the XRT+HRI performance which may be useful in preparing ROSAT observation proposals.

4.2. Point Source Sensitivity

The point source sensitivity for an observation, and therefore the required observation time, can be approached in several different ways depending upon what specific question is being asked. In all cases, the required point-source sensitivity is determined by the minimum number of source counts needed to satisfy particular statistical criteria. For example, if the scientific goal is to measure the X-ray flux from a specific object, then the appropriate signal to noise requirement might be 3. On the other hand, the determination of source existence might require a signal to noise ratio of 5 in order to avoid spurious detections due to statistical fluctuations. Three different perspectives for the determination of the required exposure for an observation are considered:

- It is desired to know the flux of a given source. In this context, Gaussian statistics are appropriate as quantitative information about the source is required, rather than a simple detection.
- It is desired to know whether a given source emits X-rays. In this context, Poisson statistics are appropriate as existence, not flux, is at issue.
- It is desired to search a field of an observation for X-ray sources. In this context either Poisson or Gaussian statistics can be used depending on the scientific goals of the observer. However, an additional aspect must be considered: the number of false detections to be expected over the search region.

4.2.1. Flux of a Source - Gaussian Statistics Case

This is the most useful case as in general not just a detection, but a measurement of the flux (or upper limit on the flux) of a source is required.

On-axis, the signal to noise ratio is given by:

$$K_{snr} = N_{src}/\left(var(N_{tot})\right)^{1/2}$$

where N_{src} is the number of source counts, and $var(N_{tot})$ is the variance in the total counts (source + background) and is typically given by $var(N_{tot}) = N_{src} + N_b$, which assumes no uncertainty in the background.

The minimum detectable source count rate corresponding to a particular signal to noise ratio is given by the relationship

$$R_{min}t = \left(K_{snr}^2/2\right) + \left(\left(K_{snr}^2/2\right)^2 + K_{snr}^2 R_b t\right)^{1/2}$$

where R_{min} denotes the minimum detectable source count rate, R_b the total background rate in the detection cell, t the observation time, and K_{snr} the desired signal to noise ratio (snr) on the flux measurement. This is derived by combining the equations defining the snr and variance, and using the additional relation, counts = rate x time. The standard estimate of R_b uses the last entry of Table 5, 1.1×10^{-6} $counts\ s^{-1}\ arcsec^{-2}$, multiplied by the area of the detection cell (in $arcsec^2$).

Given a desired s/n and a countrate, one can also solve for the time required to achieve a particular s/n for a particular source:

$$t = K_{snr}^2 \left[1/R + R_b/R^2 \right]$$

where R is the countrate of the source.

As an illustrative example (see Figure 26), we show the point source sensitivity for $K_{snr} = 5$ versus observing time for a source with a power law spectrum.

That is, we assume a point source with a power law spectrum of energy index 0.5 similar to the extragalactic X-ray background. A hydrogen column density of 5×10^{20} cm^{-2} is used. Notice that the sensitivity increases linearly with observing time for short observations where there are virtually no background counts in the detection cell. For observations that are long enough for background to be significant, longer than about $10^5 s$, the sensitivity increases only as the square root of the observation time.

In general, the conversion from HRI counts to energy flux depends on the spectrum of the X-ray source. For the power law spectrum characterized by the parameters given above, this conversion is given by: 1 count s^{-1} = 1.06×10^{-10} erg cm^{-2} s^{-1} in the energy band 0.1 to 2.4 keV. The following section discusses the conversion from energy flux to count rate in more detail.

Off-axis, sensitivity estimates must take into account the cell size from the off-axis PSF (cf. Section 3.2). The cell size can be taken as the 50% power radius, i.e., a square region where 50% of the source counts will fall. The background rates must also be scaled to the new cell size.

The vignetting correction in Figure 3.2.1 can be used to scale down the number of counts detected from off-axis sources due to the decrease in telescope area; since the HRI field of view is limited, the slight energy dependence of the vignetting correction can usually be neglected for feasibility purposes.

4.2.2. Existence of a Source - Poissonian Statistics Case

The typical HRI background in on-axis detection cells ($\sim 5'' \times 5''$) is of order unity or lower for most HRI observations ($\lesssim 100$ ks), and therefore in the range where Poisson statistics are appropriate for source-detection analysis. For example, the number of background counts expected in a detection cell for a 20 ks observation is 0.55. A 5σ detection of a source using Poissonian statistics would then require 7 counts, for a count rate of 3.5×10^{-4} counts s^{-1} in the detection cell, a total count rate of 7.0×10^{-4} counts s^{-1}. The count rate of the source, however, is known to less than 3σ. In lieu of an analytic function (of which none exists), Figure 27a displays a contour plot of limiting (total) count rate for a source detection on a grid of significance (sigma) and exposure. The plot was generated for the on-axis detection cell and assumes the nominal background rate. Figure 27b shows the same information for a region of interest $10'$ off axis where the detection cell is $\sim 12'' \times 12''$ and the background count rate $\sim 1.6 \times 10^{-4}$ counts s^{-1}. Off axis, the same considerations of vignetting correction and larger detection cells as for the Gaussian case must be taken. The conversion between count rate and flux is the same as above.

4.2.3. Detection of Previously Unknown Sources Over a Field

If one wishes to survey a field for X-ray sources, one should consider the number of false sources expected in the region. If one is interested primarily in source detection (Poisson statistics case), one can obtain a rough estimate of the number of false sources by considering the number of independent detect cells in the region of interest. For example, in the inner $10'$ diameter region, there are approximately 10000 $5'' \times 5''$ detect cells. Setting the detection significance level at 10^{-4} would therefore produce, on average, one false source in the region. One must be careful, however, in applying this analysis to source detection algorithms which use sliding detect cells, since adjacent cells are not independent. In such cases, the false source rate may best be determined by simulations. The PROS task QPSIM may be used to simulate QPOE files containing blank HRI fields with given background rates.

In the Gaussian statistics case, there is no simple way, a priori, to estimate the number of false sources from the count rate significance threshold. In this case, simulations are necessary, and were, in fact, performed to set detection thresholds for the ROSAT HRI Level 1 software in the

SASS system. It was determined there that for typical HRI exposures, detection thresholds of $2-3\sigma$ resulted in approximately 1 false source per field in each cell size used. Based on experience with the Einstein Observatory, a more conservative limit, say $3-4\sigma$ might be appropriate. Again, observers may wish to perform their own simulations if this point is crucial to their feasibility analysis.

4.3. Expected Count Rates

*********************** WARNING ***************** WARNING **************************

With the 1997 May revision, this section has been rewritten in order to give ECF tables based on the current version of the IRAF/PROS software and effective area tables (PROS 2.4); and to provide conversion factors which refer to the total countrate of a source (not the "50% detection cell"). Therefore, it is up to the user to apply the appropriate vignetting, scattering, and other corrections to the countrate.

****

The expected HRI count rates depend sensitively on the assumed incident spectrum, which is not well known for many sources. In general, the convolution of the effective area and incident spectrum needs to be calculated to predict the HRI counting rate. Since the effective area is not a simple analytic function, the convolution is not straight-forward. In order to facilitate count rate calculations we provide a series of tables and corresponding figures which give the energy-to-counts conversion factor (ECF) for several spectral models and various spectral parameters.

Tables for computing the expected count rates in the ROSAT HRI were generated for four spectral models. These are:

1. Power Law Spectrum, where α is the energy index.
2. Thermal Bremsstrahlung (Exponential plus Gaunt Factor) Spectrum, where kT is in keV.
3. Raymond-Smith Plasma Spectrum where kT is in keV.
4. Blackbody Spectrum, where kT is in keV.

For each spectral model we calculate the factor by which the unabsorbed source flux in the $0.1-2.4$ keV band measured in cgs units ($erg\ cm^{-2}\ s^{-1}$) has to be multiplied in order to obtain the expected HRI on-axis count rate. The conversion factor is a function of the intrinsic source spectrum (characterized by α or kT), and the interstellar absorption column density N_H.

The ECF values were derived by multiple runs of the task 'hxflux' in IRAF/PROS vs 2.4. The effective area curve is that included in the PROS release, and differs in small ways from that used previously: although the same calibration points were used, the model fits were slightly different. Therefore, do not expect to find perfect agreement with the effective area shown in the figure and table of the section on effective area.

Except for the Raymond-Smith spectra (Table 8c), most entries in the new tables agree with their previous counterparts to 10% or better. Significant differences occur for soft spectra with non-negligable column densities. We believe this results from the poorly known effective area at soft energies, not from software problems. In the extreme case of high absorption and extremely soft spectra, the model 'presented to' the mirror/detector mimics a delta function in energy, and it is clear that markedly different results can be obtained form small differences in the fit to the effective area.

The newly derived ECF factors for the Raymond-Smith spectra are within 10% of the previous values only for kT $>$ 3 keV and for kT close to 0.3 keV. We suspect that the larger changes for other temperatures arise because of differences in the version of the RS tables. The Raymond-Smith tables resident in PROS 2.4 are those which were new in 1992 Oct (PROS release 2.1); the previous ECF values used an older version (circa 1990.5).

The tables should be used as follows:

1. Estimate the **un** absorbed source flux $F_{S,0}$ in cgs units ($ergs\ cm^{-2}\ s^{-1}$) in the ROSAT pass band 0.1 - 2.4 keV. This is the flux which would have been incident on the Earth in the absence of any absorption.
2. Estimate the interstellar absorption column density.

3. With the assumed values of N_H and spectral parameter (α or kT) read the resulting energy-to-counts conversion factor ECF.
4. Multiply $F_{S,0}$ and ECF to obtain the expected ROSAT HRI count rate.

$$\text{counts/sec} = \text{ECF} * F_{S,0}$$

Table 8a. Power Law
ROSAT HRI Energy to Count Conversion Factors
log(N$_H$)

α	**0.0**	**18.0**	**18.7**	**19.0**	**19.7**	**20.0**	**20.7**	**21.0**	**21.7**	**22.0**	**22.7**	**23.0**
0.0	2.63e10	2.62e10	2.60e10	2.58e10	2.43e10	2.30e10	1.89e10	1.64e10	7.80e9	4.00e9	1.61e8	1.04e7
0.5	3.02e10	3.00e10	2.95e10	2.90e10	2.61e10	2.38e10	1.75e10	1.48e10	6.50e9	3.18e9	1.14e8	7.03e6
1.0	3.39e10	3.36e10	3.27e10	3.18e10	2.64e10	2.28e10	1.42e10	1.14e10	4.56e9	2.12e9	6.78e7	4.00e6
1.5	3.66e10	3.62e10	3.48e10	3.32e10	2.53e10	2.02e10	9.93e9	7.40e9	2.65e9	1.17e9	3.28e7	1.85e6
2.0	3.78e10	3.73e10	3.54e10	3.33e10	2.30e10	1.70e10	6.22e9	4.18e9	1.30e9	5.41e8	1.33e7	
2.5	3.80e10	3.72e10	3.48e10	3.21e10	2.04e10	1.39e10	3.71e9	2.15e9	5.69e8	2.21e8	4.70e6	
3.0	3.72e10	3.64e10	3.35e10	3.05e10	1.77e10	1.13e10	2.21e9	1.07e9	2.31e8	8.32e7	1.53e6	

Table 8b. Thermal Bremsstrahlung
ROSAT HRI Energy to Count Conversion Factors
log(N$_H$)

kT	**0.0**	**18.0**	**18.7**	**19.0**	**19.7**	**20.0**	**20.7**	**21.0**	**21.7**	**22.0**	**22.7**	**23.0**
0.03	3.13e10	3.02e10	2.64e10	2.26e10	8.98e9	4.00e9	1.49e8	1.33e7				
0.05	3.65e10	3.57e10	3.25e10	2.93e10	1.52e10	8.51e9	6.58e8	8.91e7				
0.10	4.14e10	4.08e10	3.84e10	3.58e10	2.27e10	1.49e10	2.14e9	5.77e8	2.14e7	2.46e6		
0.30	3.85e10	3.81e10	3.67e10	3.51e10	2.67e10	2.09e10	8.08e9	5.17e9	1.19e9	3.84e8	3.97e6	
0.50	3.67e10	3.65e10	3.55e10	3.43e10	2.79e10	2.34e10	1.24e10	9.20e9	2.85e9	1.11e9	1.98e7	
1.00	3.44e10	3.42e10	3.35e10	3.28e10	2.84e10	2.51e10	1.65e10	1.33e10	5.03e9	2.22e9	5.80e7	3.12e6
3.00	3.09e10	3.08e10	3.03e10	2.99e10	2.71e10	2.49e10	1.85e10	1.55e10	6.66e9	3.20e9	1.07e8	6.36e6
5.00	2.99e10	2.98e10	2.95e10	2.90e10	2.65e10	2.45e10	1.87e10	1.58e10	6.99e9	3.40e9	1.20e8	7.25e6

Table 8c. Raymond-Smith
ROSAT HRI Energy to Count Conversion Factors
log(N$_H$)

kT	**0.0**	**18.0**	**18.7**	**19.0**	**19.7**	**20.0**	**20.7**	**21.0**	**21.7**	**22.0**	**22.7**	**23.0**
0.01	4.21e10	3.86e10	2.77e10	1.89e10	2.09e9	3.50e8						
0.03	2.79e10	2.66e10	2.21e10	1.80e10	5.57e9	2.06e9	4.53e7	3.93e6				
0.05	3.65e10	3.55e10	3.19e10	2.84e10	1.39e10	7.21e9	3.57e8	4.68e7				
0.10	4.54e10	4.47e10	4.22e10	3.96e10	2.75e10	1.92e10	3.30e9	1.03e9	3.78e7	4.03e6		
0.30	3.59e10	3.58e10	3.54e10	3.49e10	3.19e10	2.94e10	2.12e10	1.66e10	3.78e9	8.64e8	4.66e6	
0.50	4.18e10	4.16e10	4.13e10	4.08e10	3.86e10	3.70e10	3.03e10	2.51e10	6.90e9	1.81e9	1.52e7	
1.00	3.71e10	3.70e10	3.64e10	3.57e10	3.26e10	3.09e10	2.57e10	2.22e10	8.84e9	3.47e9	6.08e7	3.43e6
3.00	3.12e10	3.11e10	3.07e10	3.03e10	2.78e10	2.59e10	2.01e10	1.72e10	7.70e9	3.69e9	1.14e8	6.78e6
5.00	3.00e10	2.99e10	2.95e10	2.92e10	2.68e10	2.50e10	1.94e10	1.65e10	7.40e9	3.60e9	1.22e8	7.44e6

Table 8d. Blackbody
ROSAT HRI Energy to Count Conversion Factors
log(N_H)

kT	**0.0**	**18.0**	**18.7**	**19.0**	**19.7**	**20.0**	**20.7**	**21.0**	**21.7**	**22.0**	**22.7**	**23.0**
0.03	4.07e10	4.00e10	3.72e10	3.42e10	1.96e10	1.16e10	9.43e8	1.17e8				
0.05	4.62e10	4.56e10	4.37e10	4.14e10	2.90e10	2.03e10	3.14e9	7.70e8	1.33e7			
0.10	3.43e10	3.41e10	3.33e10	3.24e10	2.68e10	2.21e10	9.35e9	5.63e9	8.08e8	1.71e8		
0.30	3.25e10	3.24e10	3.23e10	3.22e10	3.14e10	3.06e10	2.64e10	2.30e10	1.00e10	4.62e9	1.20e8	6.08e6
0.50	2.55e10	2.55e10	2.54e10	2.54e10	2.50e10	2.46e10	2.22e10	1.99e10	1.01e10	5.29e9	2.06e8	1.26e7
1.00	1.89e10	1.89e10	1.89e10	1.89e10	1.87e10	1.84e10	1.70e10	1.55e10	8.64e9	4.84e9	2.42e8	1.66e7
3.00	1.54e10	1.54e10	1.54e10	1.54e10	1.53e10	1.51e10	1.40e10	1.29e10	7.54e9	4.40e9	2.48e8	1.81e7
5.00	1.49e10	1.49e10	1.49e10	1.48e10	1.47e10	1.46e10	1.36e10	1.25e10	7.35e9	4.32e9	2.49e8	1.83e7

4.3.1. Blackbody spectrum example

The expected count rate from a source with a blackbody spectrum (perhaps a neutron star) needs to be estimated. The source has $L_x = 10^{33}$ $ergs\ s^{-1}$ in the ROSAT energy band (0.1 to 2.4 keV), and is at a distance of 2 kpc with $N_H = 1 \times 10^{21}$ cm^{-2} ($\log(N_H) = 21$). The assumed temperature is equivalent to 0.1 keV. The unabsorbed flux for this source is $F_{S,0} = 2.09 \times 10^{-12}$ $ergs\ cm^{-2}\ s^{-1}$. From Table 8d or Figure 31, the appropriate ECF is 5.63×10^9, and the expected count rate is 0.012 $ct\ s^{-1}$. We estimate that a detection of this source at the 5σ level will require an observation time of about 4,000 seconds.

4.3.2. Power-law spectrum example

Consider a distant AGN with a power law spectrum of energy slope 0.5 which is at a luminosity distance of 1000 Mpc and is viewed through an absorption column of 5×10^{20} cm^{-2} ($\log(N_H) = 20.7$). The AGN luminosity in the ROSAT band is $L_x = 10^{44}$ $ergs\ s^{-1}$. We want to determine how long an observation is required for a 10σ detection. The unabsorbed flux is $F_{S,0} = 8.37 \times 10^{-13}$ $ergs\ cm^{-2}\ s^{-1}$. The ECF for this spectral model is taken from Table 8a or Figure 28, it is 1.75×10^{10}, which gives a count rate 0.0146 $ct\ s^{-1}$. Using the sensitivity formula from section 4.2.1 with R=0.0073 $ct\ s^{-1}$ (50% of the total so as to refer to the 5"x5" detect cell), we calculate that the observation time needed to detect this source at the 10σ level is about 13,700 seconds.

4.3.3. Raymond-thermal spectrum example

What is the conversion factor from counts per second to energy flux for a particular spectrum? For example, consider a Raymond-Smith Plasma with a temperature corresponding to 1 keV and a column of 5×10^{21} cm^2 ($\log(N_H) = 21.7$). The ECF for this spectral model is taken from Table 8c or Figure 30, it is 8.84×10^9. That is, a flux of 1×10^{-11} $ergs\ cm^{-2}\ s^{-1}$ in the ROSAT energy band (0.1 to 2.4 keV) will give a count rate of 0.0884 $ct\ s^{-1}$ in the HRI. Inverting this relationship gives the result that 1 $ct\ s^{-1} = 1.13 \times 10^{-10}$ $ergs\ cm^{-2}\ s^{-1}$.

4.4. Time Variability Studies

The time variability of X-ray emission can be studied with the HRI since each detected photon has its time of arrival recorded by the detector. The accuracy of this time is limited by the electronic resolution of the HRI processor which is 61 μs relative to the ROSAT spacecraft clock. The relative arrival times of photons during a single observation is accurate to this value. The absolute accuracy of the ROSAT spacecraft clock, and its conversion to UT, is expected to be a few milliseconds.

The HRI has a processing dead time during which events may not be counted which varies between 0.36 and 1.35 ms per event. The variation is discussed in section 4.3.2.5 and depends on the fine position of the event. Thus there is a dead time correction that needs to be made for calculating the true event rate from a source. A mean dead time of $\rho = 0.81$ ms can be used for this purpose, and the true rate is then given by: $n_t = n(1 + n\rho)$, where n is the observed rate.

Due to the telescope wobble and the small variations in the QE of the HRI on spatial scales of a few arcminutes (see Figure 13), the count rate of a source can vary by 5% between the extremities of a wobble. This can produce a low amplitude source variability on a time scale of approximately 100-400 s in some sources.

As for the PSPC, the HRI observations are typically interrupted once per orbit, and sometimes as much a three times per orbit. Typical continuous viewing times for a source will be about 2000 s, with some cases lasting up to 4000 s. Long term monitoring of sources on time scales of weeks of more will be limited by the solar view constraints of the satellite. This limits source accessibility to about one month every six months for a source in the elliptic plane, with greater access time for sources closer to the ecliptic poles.

4.5. Comparison to the *Einstein* HRI

Comparisons between the *Einstein* and ROSAT HRI's must account for the different detector photocathodes and band passes of the two telescopes. As shown by the effective area comparison given in Figure 11.8 of Appendix F, the HRI effective area of ROSAT exceeds that of *Einstein* over most of the ROSAT energy band (because of the increased area of the ROSAT mirrors and the greater sensitivity of its CsI photocathode). As can be seen from Table 3, observed ROSAT count rates are typically a factor of 3 to 4 times those measured with the *Einstein* HRI (the values of this ratio, of course, depending upon interstellar absorption and the intrinsic source spectra).

The better scattering performance and a smaller point spread function of the ROSAT XRT, vis a vis the *Einstein* telescope, should ultimately permit the use of a $5''$ detect cell, as assumed above for feasibility calculations, provided the aspect contribution to the PSF can be reduced.

References

Arp, H.C. 1995, Astron. Astrophys., 294, L45.

Silverman, J.D., Kearns, K.E., and Harris. D.E. 1996, ASP Conf. Series 101, "Astronomical Data Analysis Software and Systems V" G. H. Jacoby and J. Barnes, eds. page 120.

Zombeck, M.V., David, L.P., Harnden, Jr., F.R., and Kearns, K., Proc. SPIE, Vol. 2518, pp. 304-321, 1995.

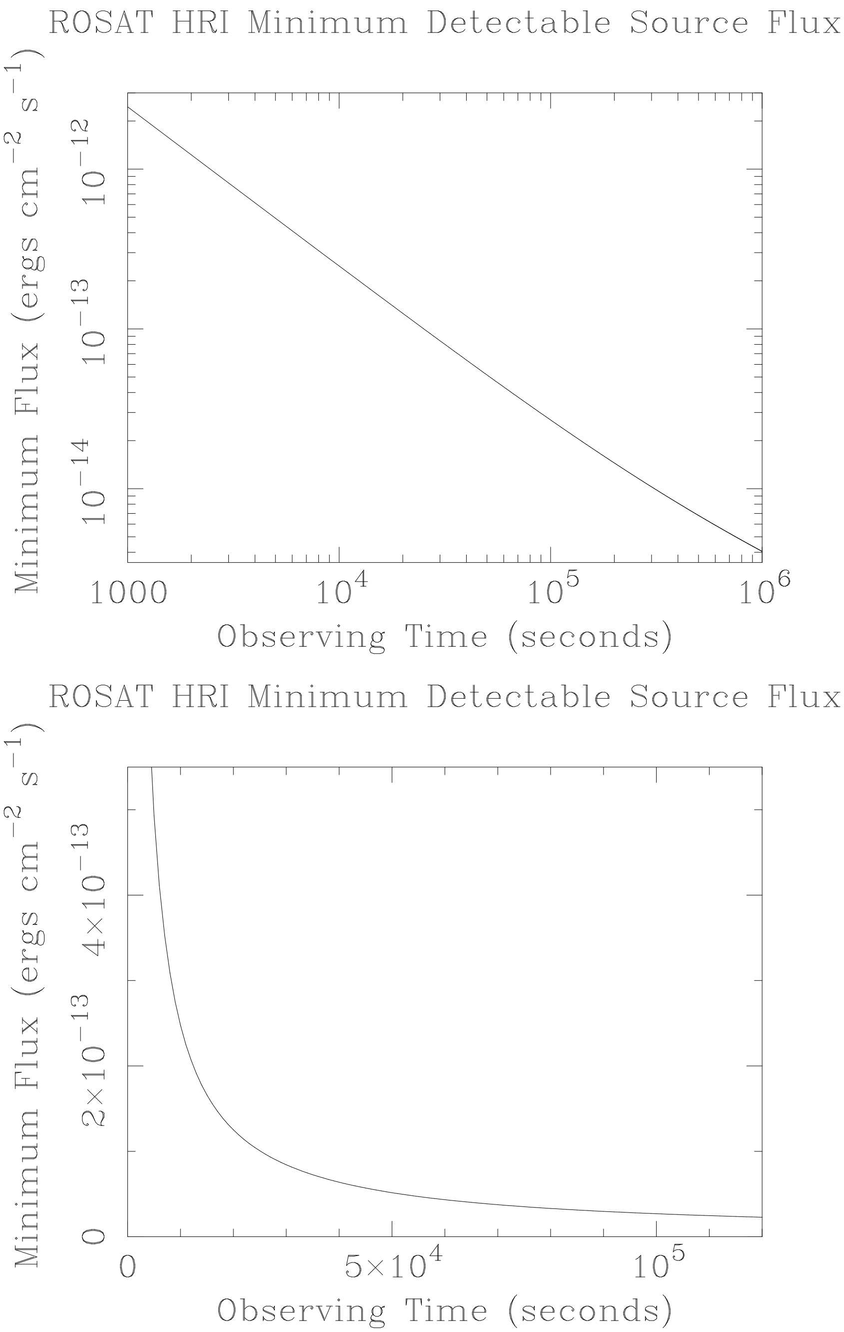

Fig. 26. The relationship between R and t for a snr of 5, with the standard background rate, alpha=0.5 and log NH=20.7. (a) a log-log plot; (b) the same, but for a linear scale.

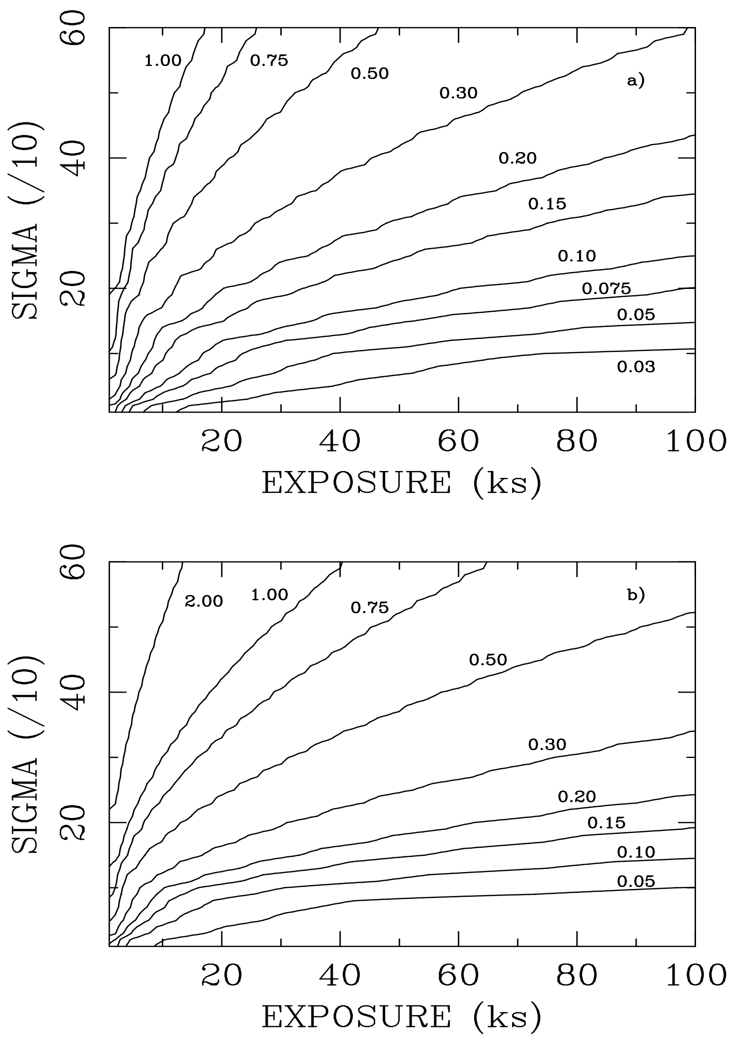

Fig. 27. The relation between source count rate, statistical significance, and exposure for an HRI observation using Poisson statistics is shown. The contour plots show the source count rate in units of 10^{-3} counts s^{-1} versus exposure in ks and sigma (a value for σ of 50 refers to 5σ). Plot a) is for the on-axis case, plot b) is for $10'$ off axis.

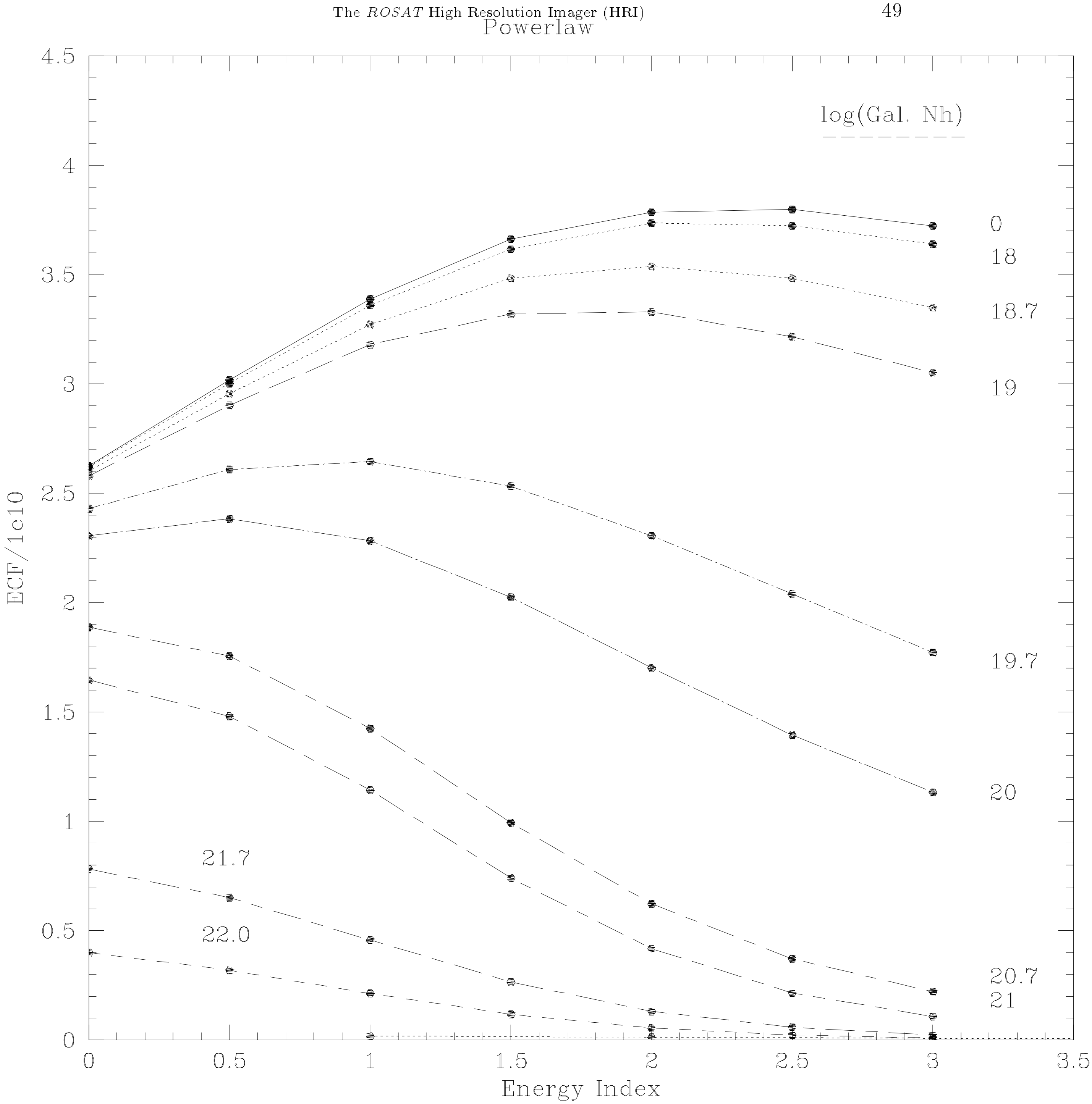

Fig. 28. The ECF (energy-to-counts conversion factor) is plotted as a function of the energy index for the powerlaw spectral model. The values are shown for a range of absorbing column densities ($\log(N_H)$).

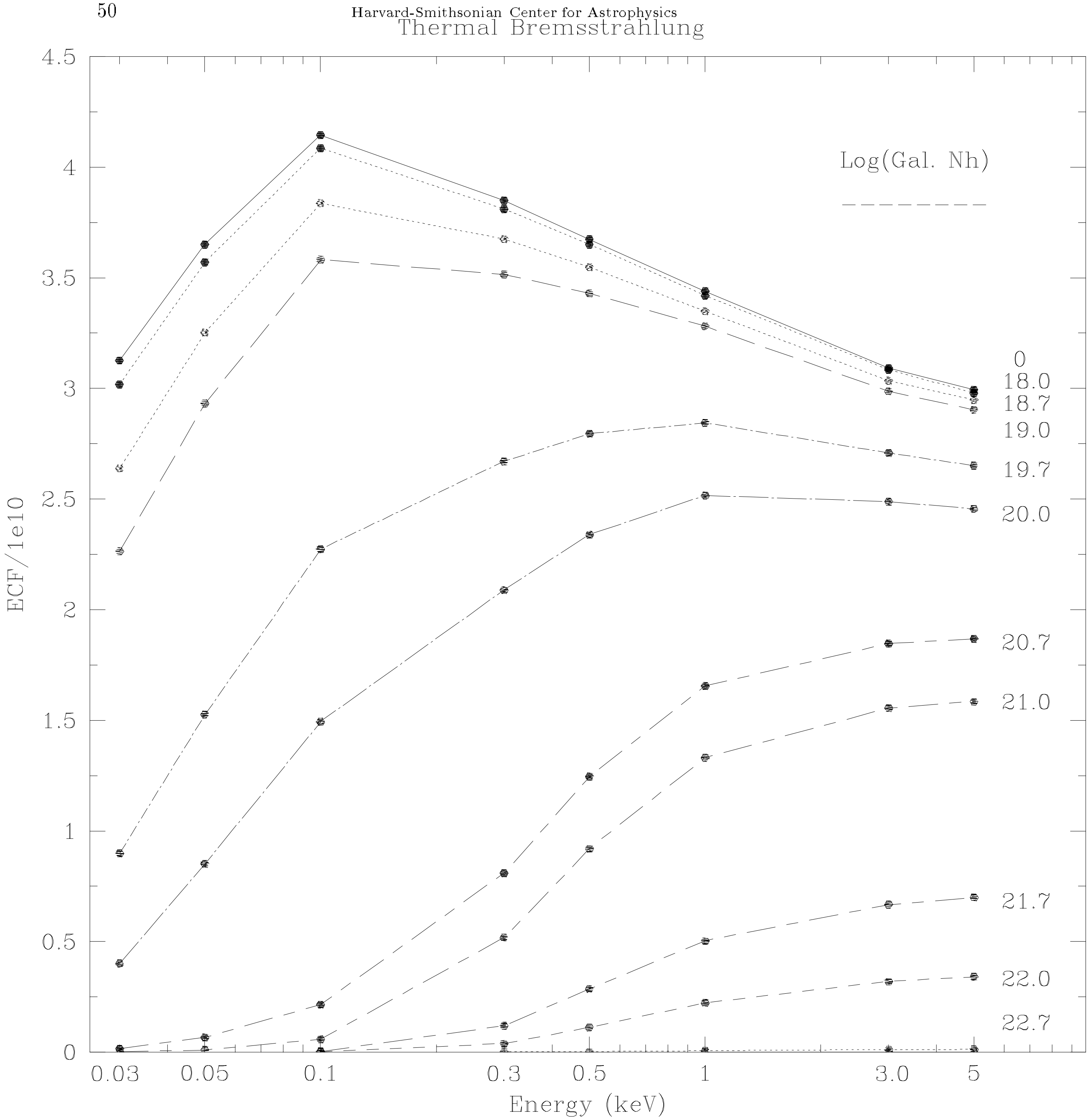

Fig. 29. The ECF (energy-to-counts conversion factor) is plotted as a function of the temperature (Log(kT)) for a Thermal Bremsstrahlung spectral model. The values are shown for a range of absorbing column densities ($\log(N_H)$).

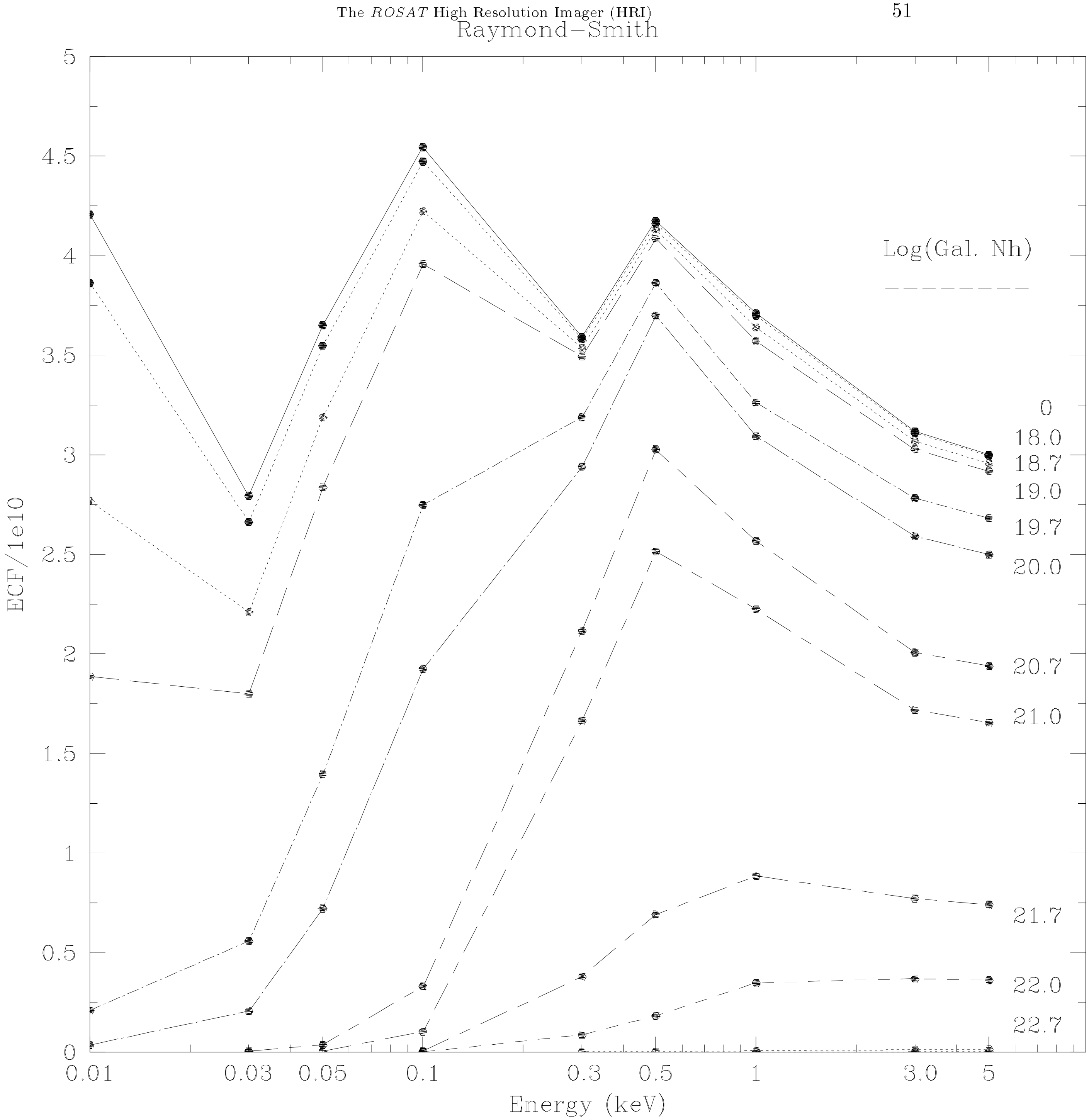

Fig. 30. The ECF (energy-to-counts conversion factor) is plotted as a function of the temperature (Log(kT)) for a Raymond-Smith spectral model. The values are shown for a range of absorbing column densities ($\log(N_H)$).

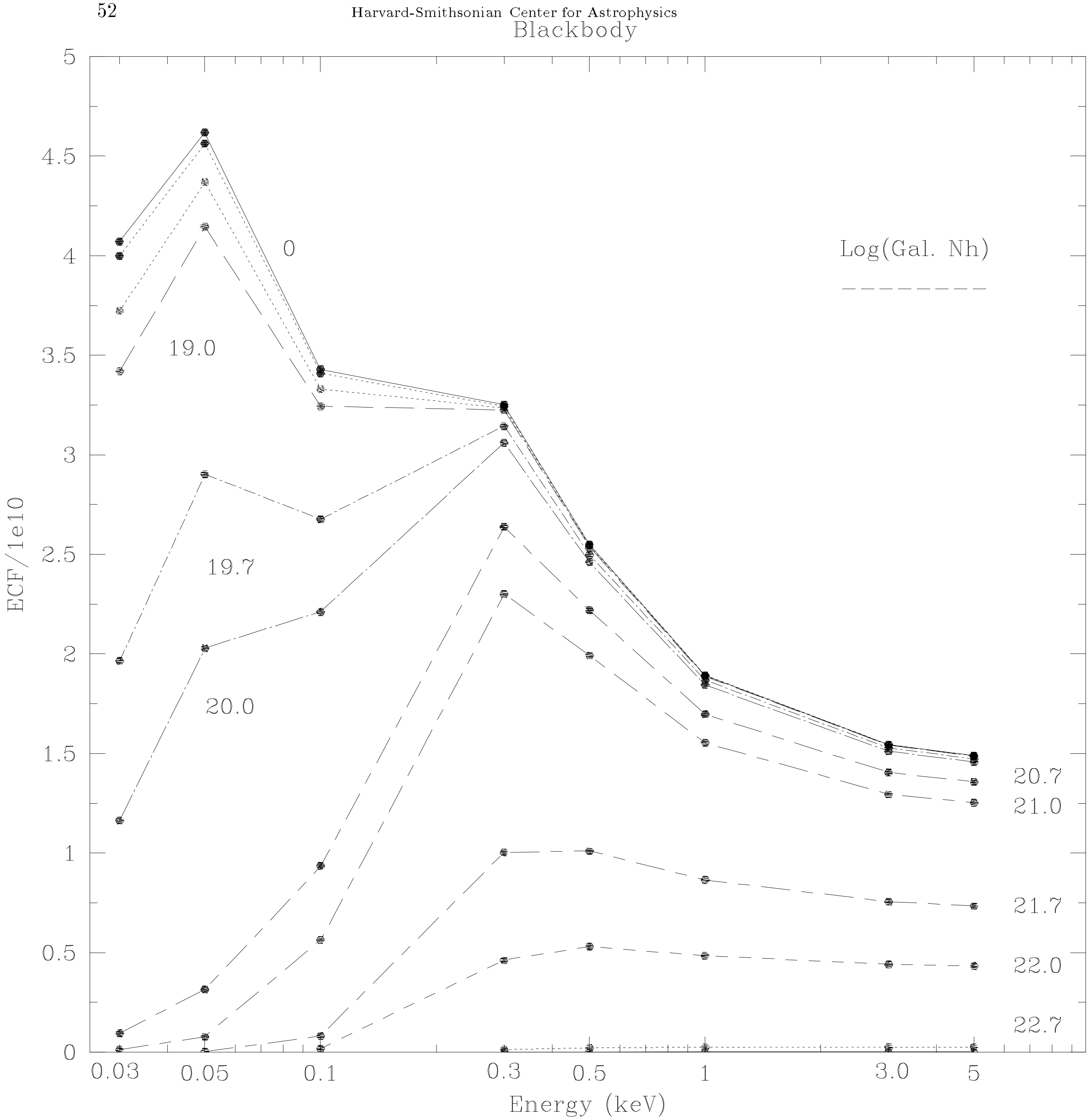

Fig. 31. The ECF (energy-to-counts conversion factor) is plotted as a function of the temperature (Log(kT)) for a blackbody spectral model. The values are shown for a range of absorbing column densities (log(N_H)).